Check for updates

View Article Online
View Journal

Chemical
Science

Accepted Manuscript

This article can be cited before page numbers have been issued, to do this please use: M. Lun, M. Sun, Y. Wang, G. Gong, M. Wei, Y. Su, D. Fu and Z. Liu, *Chem. Sci.*, 2026, DOI: 10.1039/D5SC10231F.

Chemical
Science

Volume 9
Number 1
7 January 2018
Pages 1-268

rsc.li/chemical-science

ISSN 2041-6539

ROYAL SOCIETY
OF CHEMISTRY

EDGE ARTICLE
Xinjing Tang *et al.*
Caged circular siRNAs for photomodulation of gene expression in cells and mice

This is an Accepted Manuscript, which has been through the Royal Society of Chemistry peer review process and has been accepted for publication.

Accepted Manuscripts are published online shortly after acceptance, before technical editing, formatting and proof reading. Using this free service, authors can make their results available to the community, in citable form, before we publish the edited article. We will replace this Accepted Manuscript with the edited and formatted Advance Article as soon as it is available.

You can find more information about Accepted Manuscripts in the Information for Authors.

Please note that technical editing may introduce minor changes to the text and/or graphics, which may alter content. The journal's standard Terms & Conditions and the Ethical guidelines still apply. In no event shall the Royal Society of Chemistry be held responsible for any errors or omissions in this Accepted Manuscript or any consequences arising from the use of any information it contains.

ROYAL SOCIETY
OF CHEMISTRY

rsc.li/chemical-science

View Article Online
DOI: 10.1039/D5SC10231F

Recent Progress in Single-phase Molecular Multiferroic Materials with Ferroelectricity and Ferroelasticity

Received 00th January 20xx,
Accepted 00th January 20xx

DOI: 10.1039/x0xx00000x

Meng-Meng Lun,[a] Meng-Meng Sun,[a] Yong-Qiang Wang,[a] Gao-Shang Gong,[a] Mao-Cai Wei,[a] Yu-Ling Su,[a] Da-Wei Fu*[b,c], Zun-Qi Liu,*[c]

Single-phase multiferroic materials, characterized by the coexistence of ferroelectricity and ferroelasticity, have garnered significant attention due to the inherent coupling between polarization and strain. This coupling offers considerable potential for applications in multistate memories, high-sensitivity sensors and energy converters. Recently, molecular multiferroic materials have emerged as a research hotspot owing to their unique advantages, including structural diversity, facile tunability, mechanical flexibility, and environmental friendliness. Notably, these molecular multiferroics typically exhibit good mechanical flexibility and a pronounced response to applied stress, which facilitates the investigation of coupling effects between polarization and strain. However, existing reviews predominantly concentrate on single ferroic properties or specific material systems, resulting in a notable scarcity of systematic overviews on molecular multiferroic materials. This review aims to provide a comprehensive overview of recent progress in multiferroic materials that simultaneously possess ferroelectric and ferroelastic orders. We summarize key experimental findings, elucidate the relationship between molecular design strategies and material performance, and explore their potential applications in flexible electronics, biomimetic sensing, and bio-integrated devices. This review is expected to shed new light on the future of this emerging field and promote cross-disciplinary cooperation and innovation in materials science, electronic engineering, biomedicine, and other related fields.

1. Introduction

Ferroic materials play significant roles in the advancement of human civilization. Among these, single-phase multiferroic materials, which exhibit both full ferroelectricity and full ferroelasticity possess significant scientific and commercial applications.[1-13] The field traces its origins to the discovery of the first molecular multiferroic, Rochelle salt ($NaKC_4H_4O_6{\cdot}4H_2O$), by Joseph Valasek in 1920. Rochelle salt exhibits coexisting ferroelectric and ferroelastic orders within the temperature range of 255-297 K, which is the earliest reported single-phase molecular multiferroic with full ferroelectric and full ferroelastic orders. [14, 15] A second example, KH_2PO_4 (KDP), was discovered in 1935, displaying both ferroelectricity and ferroelasticity below 123 K.[16] Subsequent research has uncovered additional molecular-based multiferroics.[17] A unique characteristic of these materials is the coupling between the spontaneous polarization vector and the ferroelastic strain, implying that a change in one order parameter necessarily induces a cooperative change in the other. This inherent coexistence and coupling between polarization and strain can contribute to significant piezoelectric and electrostrictive effects, thereby enabling molecular multiferroics with full ferroelectricity and full ferroelasticity to show promising applications in high-density multi-state memory, highly sensitive sensors, and intelligent actuators.[18-21]

Molecular materials offer distinct advantages, including structural diversity, rich components, and facile chemical modification and tunability.[9, 22] Molecular multiferroic materials can be constructed from a wide variety of structural building blocks, including organic cations (*e.g.*, protonated amines, quaternary ammonium salts), inorganic anions or metal centers (*e.g.*, transition metals, halide ions, cyanide groups), and flexible organic ligands. Compared to inorganic single-phase multiferroics, such as $(NH_4)_2Cd_2(SO_4)_3$, $Ni_3B_7O_{13}I$, and $Gd_2(MoO_4)_3$, which often suffer from mechanical rigidity and intrinsic brittleness, molecular multiferroics typically feature good mechanical flexibility and enable a pronounced response to applied stress. This facilitates the investigation of coupling effects between polarization and strain. Furthermore, they can be synthesized via low-temperature solution methods, exhibit good biocompatibility, biodegradability, and environmental friendliness. [23]These properties position them as a promising material platform for next-generation flexible electronics

---

[a] A School of Electronics and Information, Zhengzhou University of Light Industry, Zhengzhou 450000, China.
[b] Institute for Science and Applications of Molecular Ferroelectrics, Key Laboratory of the Ministry of Education for Advanced Catalysis Materials, Zhejiang Normal University, Jinhua 321019, China.
[c] Chemical Engineering College, Xinjiang Agricultural University, Urumqi 830052, China.

and implantable medical devices, aligning with the principles of green chemistry.[24, 25]

The intrinsic electromechanical coupling in these materials arises because the reversal of ferroelectric polarization is typically accompanied by lattice deformation and alters strain, while ferroelastic strain can facilitate the reorientation of building blocks and thereby affect the polarization state. This enables the control of mechanical response via electric fields or the modulation of polarization states via stress.[26] The coexistence of ferroelectric and ferroelastic order parameters involves intricate physical mechanisms of polarization-strain coupling, which can lead to emergent phenomena and innovative functionalities, including the negative piezoelectric effect, the electro-elastic effect, and the barocaloric effect. These capabilities enable novel applications in multi-state data storage, energy conversion, shape memory, and sensing. [27]However, several challenges hinder practical application: the number of known single-phase multiferroics remains limited, the coexistence temperature of ferroelectricity and ferroelasticity is low, the synergistic control by electric field and stress is difficult, and insufficient understanding of coupling mechanisms.

This review aims to systematically summarize recent advances in molecular single-phase multiferroics with coexisting ferroelectric and ferroelastic orders. The review begins by discussing the physical foundations and mechanisms for the coexistence and coupling of these two order parameters from the perspective of symmetry conditions. Next, key experimental techniques for characterizing ferroelectricity, ferroelasticity, and their coupling effects in molecular materials will be introduced. Subsequently, representative molecular multiferroic systems reported in recent years, including coordination compounds and organic-inorganic hybrids, will be categorized and discussed, with an analysis of their design strategies, structures, and properties. Finally, based on a summary of existing research, the review will conclude with perspectives on the current challenges and future research focus in this field.

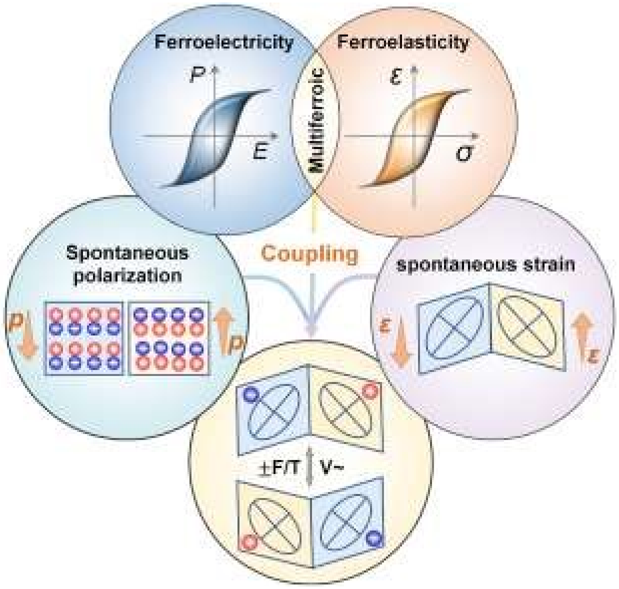

Fig.1 Schematic illustration of the coupling between ferroelectric and ferroelastic orders.

View Article Online
DOI: 10.1039/D5SC10231F

2. Fundamentals of the coexistence of ferroelectric and ferroelastic orders

2.1 The theory of full ferroelectric and full ferroelastic phase transition

Ferroelectric materials are a class of functional compounds that possesses two or more orientation states in the absence of an electric field and can be shifted from one to another of these states by an electric field. A fundamental feature of ferroelectrics is the breaking of spatial inversion symmetry, which limits these crystals to specific polar point groups:1 (C_1), 2 (C_2), m (C_s), $mm2$ (C_{2v}), 4 (C_4), $4mm$ (C_{4v}), 3 (C_3), $3m$ (C_{3v}), 6 (C_6), and $6mm$ (C_{6v}). Ferroelasticity serve as the mechanical analog of Ferroelectricity, defined for a crystal having two or more orientation states in the absence of stress that can be switched by applying external stress, with the states differing in the spontaneous strain tensor at zero stress.[28] A critical unifying principle for both ferroelectric and ferroelastic phase transitions is their inherent symmetry breaking: a transformation from a high-symmetry prototype phase to a lower-symmetry ferroic phase. This process invariably leads to the formation of distinct polarization and/or strain domains, each with specific orientations, as schematically depicted in Fig.1.[29]

In the late 1960s and early 1970s, the Japanese physicist Aizu Kêitsiro developed a systematic framework, based on phenomenological Landau theory and group theory, to classify all possible ferroic phase transitions. This theory introduced the concept of "prototype symmetry" and summarized the crystallographic allowed ferroic phase transitions, encompassing 88 species of ferroelectrics and 94 species of ferroelastics. The hallmark "Aizu notation" system describes a transition directly using the point group symbols of the high-symmetry and low-symmetry phases, with the standard notation being "[high-symmetry point group]F[low-symmetry point group]".[30-32] Among these species, 42 have been identified as fully ferroelectric and fully ferroelastic phase transition as shown in Fig. 2a, meaning all polarization and strain orientations of ferroic phase can be fully controlled by an electric field or mechanical stress. In such systems, the prototype phase must be non-centrosymmetric, though not necessarily piezoelectric (*e.g.*, the point group 432). These 42 species can be further categorized into four types based on the symmetry relations as shown in Fig. 2a: (I) 4 species of chiral polar group to chiral polar subgroup, (II) 13 species of chiral group to chiral polar subgroup, (III) 9 species of polar group to polar subgroup, (IV) 16 species of non-centrosymmetric group to polar subgroup. In such fully ferroelectric and fully ferroelastic crystals, the ferroelectricity and ferroelasticity are completely coupled: any change in the polarization vector is always accompanied by a change in the strain tensor, and vice versa. Therefore, this review specifically summarizes single-phase multiferroic materials with full ferroelectric and ferroelastic transitions.

2.2 Mechanisms driving full ferroelectric and full ferroelastic phase transition

View Article Online
DOI: 10.1039/D5SC10231F

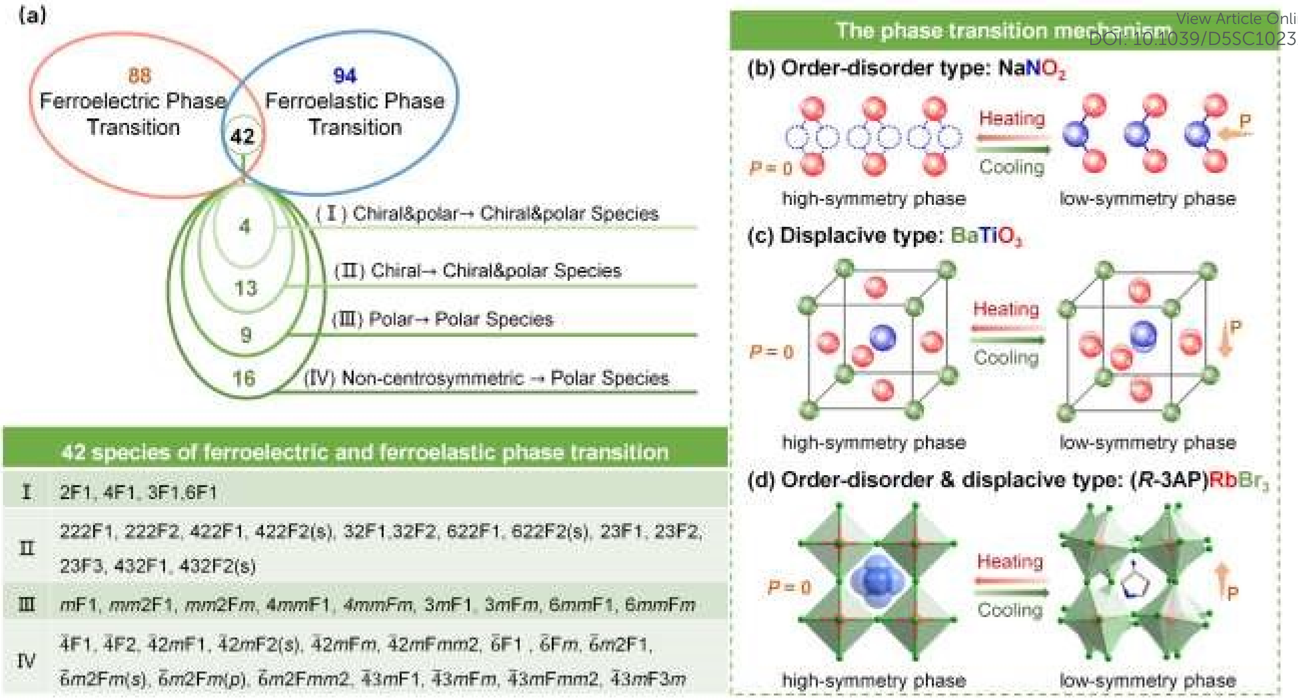

42 species of ferroelectric and ferroelastic phase transition	
Ⅰ	2F1, 4F1, 3F1.6F1
Ⅱ	222F1, 222F2, 422F1, 422F2(s), 32F1,32F2, 622F1, 622F2(s), 23F1, 23F2, 23F3, 432F1, 432F2(s)
Ⅲ	*m*F1, *mm*2F1, *mm*2F*m*, 4*mm*F1, 4*mm*F*m*, 3*m*F1, 3*m*F*m*, 6*mm*F1, 6*mm*F*m*
Ⅳ	$\bar{4}$F1, $\bar{4}$F2, $\bar{4}$2*m*F1, $\bar{4}$2*m*F2(s), $\bar{4}$2*m*F*m*, $\bar{4}$2*m*F*mm*2, $\bar{6}$F1 , $\bar{6}$F*m*, $\bar{6}$*m*2F1, $\bar{6}$*m*2F*m*(s), $\bar{6}$*m*2F*m*(p), $\bar{6}$*m*2F*mm*2, $\bar{4}$3*m*F1, $\bar{4}$3*m*F*m*, $\bar{4}$3*m*F*mm*2, $\bar{4}$3*m*F3*m*

Fig.2 (a) The subdivision of the 42 fully Ferroelectric and fully ferroelastic species. Schematic illustration of the phase transition mechanism in ferroics: (b) order-disorder type, (c) displacive type, (d) mixed order-disorder and displacive type.

The mechanisms driving full ferroelectric and full ferroelastic phase transitions in reported single-phase molecular multiferroic materials are primarily categorized into order-disorder type, displacive type, and their synergistic effects. Taking the ferroelectric-paraelectric phase transition of inorganic oxides $NaNO_2$ and $BaTiO_3$ [33], as well as organic-inorganic hybrid perovskites (*R*-3AP)$RbBr_3$ [34], as examples, illustrates these three distinct transition mechanisms as shown in Fig.2b-d.

Firstly, the order-disorder type transition is driven by the progressive alignment of molecular, ionic, or dipolar groups from a statistically disordered distribution among multiple equivalent positions into an ordered arrangement. In the high-temperature phase, dipolar or molecular units dynamically occupy multiple energetically equivalent orientations, resulting in a centrosymmetric structure. Upon cooling, these units become frozen into a specific orientation, giving rise to long-range order and symmetry breaking. As typified by $NaNO_2$, the compound transforms from a high-symmetry prototype phase to a low-symmetry ferroic phase upon cooling. This transition is predominantly driven by the "freezing" of disordered occupancies, such as the nitrogen atom within the NO_2^- anion, into an ordered state as shown in Fig.2b.

Secondly, the displacive type mechanism arises primarily from the relative displacement of ions within the lattice, generating an electric dipole moment and strain. For example, this relative displacement of O^{2-} and Ti^{4+} ions induces the spontaneous polarization in the inorganic ferroelectric $BaTiO_3$ (Fig.2c). For organic-inorganic hybrid systems, atomic displacements can lead to conformational changes in the organic moieties, thereby inducing ferroic phase transitions. Furthermore, Jahn-Teller distortions in the inorganic framework can create internal stresses that induce spontaneous strain, while simultaneously causing a separation between positive and negative charge centers, leading to spontaneous polarization.[35]

Thirdly, the phase transition mechanism in organic-inorganic hybrids generally arises from a synergistic effect combining the order-disorder transition of the organic components and the displacive transition due to Jahn-Teller distortion in the inorganic anion framework.[5] In hybrid perovskites, tilting or distortion of BX_6 octahedra generally accompanies cation ordering, further contributing to symmetry lowering and ferroic phase transitions. As illustrated in Fig.2d, the ferroic phase transition in 3D (*R*-3AP)$RbBr_3$ originates from the dynamic order-to-disorder transitions of organic cations *R*-3AP$^+$ coupled with the deformation of the inorganic framework. In such fully coupled systems, any change in the polarization vector is always accompanied by a change in the strain tensor and vice versa.

3. Characterization of molecular multiferroics with ferroelectricity and ferroelasticity

Accurately characterizing the structure, ferroelectricity, and ferroelasticity of molecular-based single-phase multiferroic materials is crucial for understanding their structure-property relationships, coupling mechanisms, and evaluating their application potential. This requires the integrated use of multiple complementary experimental techniques to probe the material's structural, electrical, and mechanical properties and their interrelations across different scales. The systematic characterization of novel molecular materials typically begins with

View Article Online
DOI: 10.1039/D5SC10231F

dielectric constant measurements and differential scanning calorimetry (DSC) to establish their definitive phase transition temperature. This initial assessment is crucial for guiding subsequent structural investigations. Single-crystal X-ray diffraction (SC-XRD) is then utilized to determine the crystallographic structures of compounds at different temperature, specifically to verify if the transition mechanism falls within the 42 fully ferroelectric and fully ferroelastic species defined by Aizu. Once this conformity is established, detailed characterization of the ferroelectric and ferroelastic behaviors proceeds.

3.1 Characterization of ferroelectricity

Characterizing ferroelectricity hinges on unequivocally demonstrating the existence of a reversible spontaneous polarization. The primary and most direct technique for this purpose is the measurement of the polarization-electric field (*P*-*E*) hysteresis loop. By applying a cyclic electric field (*E*) to the material and measuring its resulting polarization (*P*), a distinct *P*-*E* loop is generated, allowing for the determination of critical ferroelectric parameters, including remanent polarization (P_r), saturation polarization (P_s), and coercive field (E_c). For molecular crystals, the electric field is applied along the crystallographic polar axis to acquire the *P*-*E* loop. However, for small single crystals or thin films, this measurement often requires a ferroelectric tester equipped with a probe station.

Piezoresponse Force Microscopy (PFM), a technique based on Atomic Force Microscopy, enables the imaging and manipulation of ferroelectric domains at the nanoscale as shown in Fig.3a. Depending on the detection direction, PFM can be in vertical (VPFM) and lateral (LPFM) modes, corresponding to out-of-plane and in-plane piezoresponses, respectively.[36, 37] Its principle utilizes the inverse piezoelectric effect: when an AC voltage is applied to the sample surface via a conductive tip, ferroelectric domains undergo minute deformation (expansion/contraction or shear) due to the piezoelectric effect. By detecting the amplitude and phase of this mechanical response, which is synchronized with the driving voltage using a lock-in amplifier, information about the piezoresponse strength and polarization direction is obtained. The PFM amplitude image displays the distribution of ferroelectric domains, while the PFM phase image distinguishes domains with opposite polarization directions (typically showing a 180° phase difference). More importantly, by applying a DC bias voltage through the tip, the domain switching process can be observed in situ as shown in Fig.3a(I-IX). This technique is a vital tool for studying domain structure dynamics and has been used to observe vortex domain structures in molecular ferroelectric materials.[38-40] It is noteworthy that PFM demands high sample flatness, typically requiring smooth and uniform thin-film samples, which can be a limitation for materials with poor film-forming properties or whose thin-film phases differ from the bulk structure.

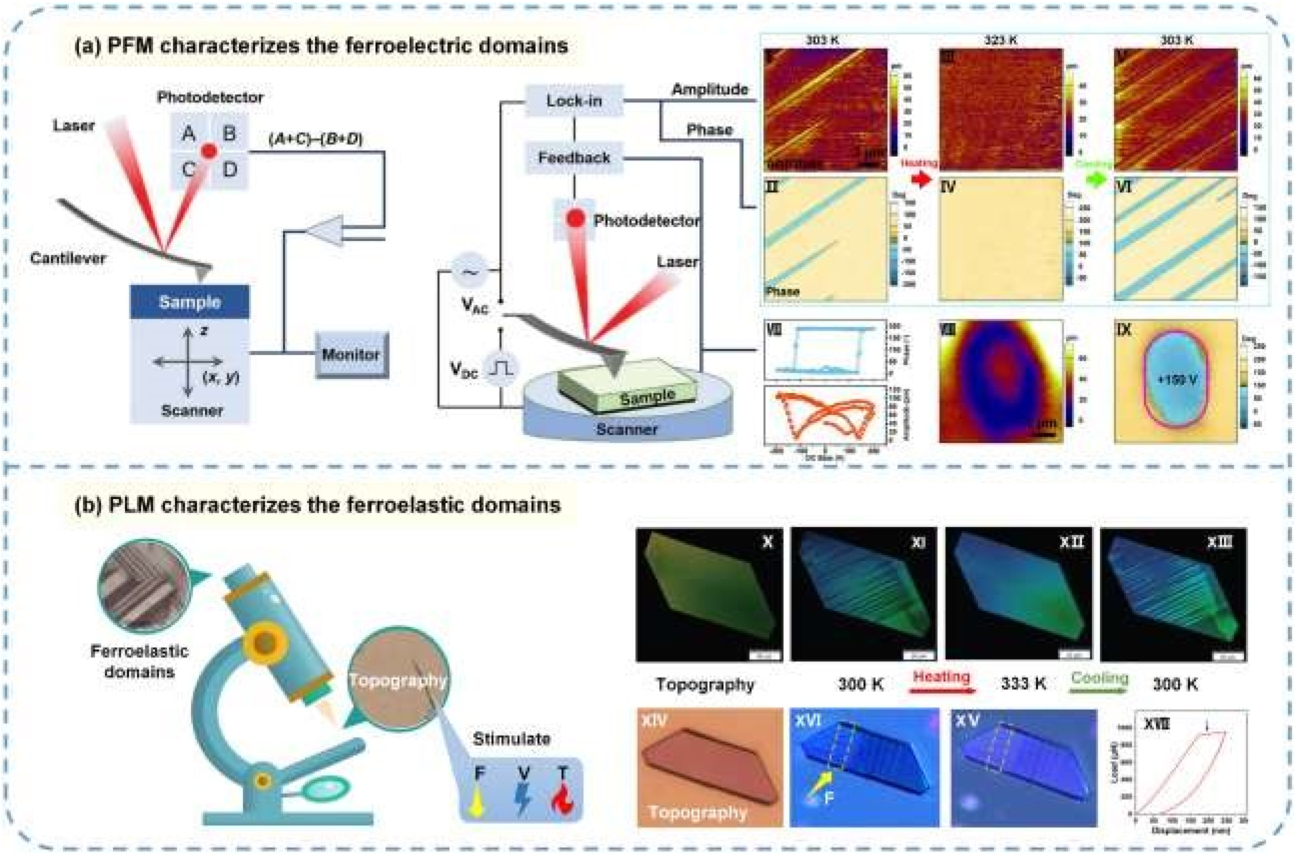

Fig.3 (a) Configurations of a typical PFM system and the PFM setup. The evolution of ferroelectric domains for the molecular multiferroic material [Fe^{II}(C$_8$-F-pbh)$_2$] with temperature and electric field is illustrated in (I-IX). (b) Schematic illustration of ferroelastic domain characterization using PLM. The evolution of ferroelastic domains for Fe^{II}(C$_8$-F-pbh)$_2$ with temperature and stress. Reproduced from ref. [36] and [41] with permission from Elsevier and Wiley, Copyright 2015 and 2024.

View Article Online
DOI: 10.1039/D5SC10231E

An indirect method to measure ferroelectricity is the pyroelectric current measurement, which leverages the pyroelectric effect. When a ferroelectric material undergoes a temperature change (ΔT), a charge (ΔQ) is released due to the variation of P_s with temperature. By cooling the sample from the paraelectric phase to the ferroelectric phase under two opposite poling fields and then heating it back to the paraelectric phase at a constant rate, the observation of a pair of opposite current peaks near the phase transition temperature proves that the spontaneous polarization can be reversed by an external field. Simultaneously, the temperature dependence of the spontaneous polarization can be calculated from the pyroelectric data.

3.2 Characterization of ferroelasticity

Ferroelasticity originates from a symmetry-breaking structural transition that produces a spontaneous strain tensor. The different orientations of strain states lie in different ferroelastic twin domains. The core of characterizing ferroelasticity lies in demonstrating the existence of the spontaneous strain that can be reversed by an applied mechanical stress. The direct method is the measurement of the stress-strain (ε-σ) hysteresis loop, where applying a cyclic stress and measuring the strain response can get a typical ε-σ loop. However, this mechanical testing poses significant challenges for molecular ferroelastics, as bulk crystals often have limited stress tolerance.

The polarized light microscopy (PLM) offers a non-contact, non-destructive method for observing ferroelastic domains. Because the spontaneous strain tensor is rigidly coupled with the optical indicatrix, the observation of birefringent domains normally indicates the presence of a ferroelastic phase.[42-46] When a material is in its low-symmetry ferroelastic phase, different domain variants (also known as twin domains) possess distinct orientations of the optical indicatrix due to lattice distortion. Due to different crystallographic axis orientations, these domain regions exhibit different optical anisotropies as shown in Fig.3b. When linearly polarized light passes through these anisotropic regions, the difference in refractive indices causes a phase shift, altering the polarization state of the light. Therefore, under crossed polarizers light, the alternating bright and dark regions correspond to the ferroelastic domains with distinct strain tensors. In contrast, the material in its high-symmetry paraelastic phase shows uniform contrast under crossed polarizers. Researchers typically perform in-situ observations of domain evolution with temperature under crossed polarizers, where the appearance and disappearance of domains across the phase transition serve as strong evidence for ferroelasticity (Fig.3b(X-XIII)). Furthermore, applying a stress to the sample while under observation allows for the in-situ monitoring of ferroelastic domain wall motion as shown in Fig.3b(XIV-XV). This method provides the most intuitive and convenient approach for observing ferroelastic domains, applicable to both high-quality bulk single crystals and thin films, provided the sample surface is sufficiently flat.[47] In nanoscale systems, atomic force microscopy (AFM) and piezoresponse force microscopy (PFM) can also be employed to visualize ferroelastic domain structures and domain wall motion.

3.3 Characterization of ferroelectric-ferroelastic Coupling

The characterization of the coupling between ferroelectricity and ferroelasticity in single-phase molecular multiferroics has primarily been reported using PFM. This involves observing changes in ferroelectric domains while applying mechanical stress or detecting surface topographic changes via an atomic force microscope tip while applying an electric field. Significantly, for materials possessing both full ferroelectricity and full ferroelasticity, their ferroelectric domains are inherently identical to their ferroelastic domains. This direct correspondence ensures that any modification of the polarization vector P is always reciprocally linked to a change in the strain tensor ε. To advance the understanding of this coupled effect, our group has recently devised a novel technique: applying an electric field to the sample while conducting in-situ observation of ferroelastic domain evolution using PLM.[48] This method confirmed the coupled effect between ferroelectric and ferroelastic domains in the 2D multiferroic hybrid perovskite (cyclohexanemethylaminium)$_2$PbCl$_4$, enabling the demonstration of electric-field-induced strain in the molecular multiferroic system.

Table 1 The reported single-phase molecular multiferroic materials

Compound	n-D	component	Phase transition	Polar/ strain axis	P_s (μC·cm^{-2})	ε	Ref.
NaKC$_4$H$_4$O$_6$·4H$_2$O (Rochelle salt)	0D	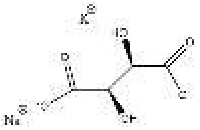	**222F2** ($P2_12_12_1$-$P2_1$-$P2_12_12_1$, T_{c1} = 297 K, T_{c2} = 255 K)	2	0.25		14
KH$_2$PO$_4$ (KDP)	0D	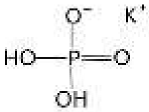	$\mathbf{\bar{4}2mFmm2}$ ($I\bar{4}2\mathrm{d}-Fdd2$, T_c = 123 K)	2	4.8		16
(R)-BINOL-DIPASi (BINOL= 1,1'-bi-2-naphthol)	0D	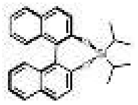	**2F1** ($P2_1$-$P1$, T_c = 362 K)	2	1.6	0.027	49

View Article Online
DOI: 10.1039/D5SC10231F

(*S*)-BINOL-DIPASi (BINOL= 1,1'-bi-2-naphthol)	0D	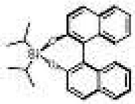		**2F1** ($P2_1$-$P1$, T_c = 363 K)	2	1.7	0.027	49
$Fe^{II}(C_8\text{-F-pbh})_2$ (C_8-F-pbh = (1*Z*,*N′E*)-3-F-4-(octyloxy)-*N′*-(pyridin-2-ylmethylene) benzo-hydrazonate)	0D	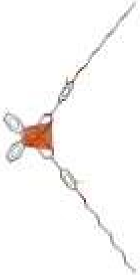		**222F2** ($P2_12_12_1$-$P2_1$, T_c = 318 K)	2	0.15		41
$[(C_6H_5)_3PCH_3]FeBr_4$	0D		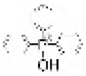	**222F2** ($P2_12_12_1$-$P2_1$, T_c = 275 K, T_N = 11 K)	2			50
PH_4FeBr_4	0D		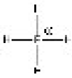			10.7	>0.4	51
[RFAO][ReO_4] (RFAO = (4*R*,5*R*)-4-fluoro-1 azabicyclo[3.2.1]octane)	0D	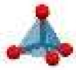		**222F2,432F2** ($P2_1$-$C222_1$-$P432$,T_{c1}=350 K,T_{c2}=463 K)	1	3.64		52
[SFAO][ReO_4] (SFAO = (4*S*,5*S*)-4-fluoro-1 azabicyclo[3.2.1]octane)	0D	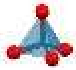		**222F2,432F2** ($P2_1$-$C222_1$-$P432$,T_{c1}=350 K,T_{c2}=463 K)	1	3.81		52
$(C_4H_8NH_2)_3[SbCl_5]$ ($C_4H_8NH_2^+$ = pyrrolidinium)	1D	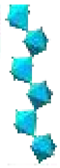	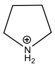	***mmmFmm2, mm2Fm, mm2F2*** ($Pmnb$-$Pmn2_1$-Pn-$P2_1$ T_{c1} = 252 K， T_{c2} = 247 K， T_{c3} = 231 K)	1, 2, 2	0.16 (217 K)		53
[FPM][$Fe_3(\mu_3\text{-}O)(\mu\text{-}O_2CH)_8$] ($FPM^+$ = 3-(3-formylamino-propyl)-3,4,5,6-tetrahydropyrimidin-1-ium)	1D			***mm2Fm*** ($Pca2_1$-Cc-$Cmc2_1$, T_{c1} = 426 K， T_{c2} = 365 K)	2	c-axis 4.64 (250 K) 4.55 (395 K) 4.46 (433K) a-axis 4.01 (395K)	0.02369 (365 K) 0.02385 (426 K)	54
[*R*-EQ]PbI_3 (*R*-EQ^+ = (*R*)-*N*-ethyl-3-quinuclidinol)	1D			**622F2(*s*)** ($P6222$-$P2_1$-$P2_1$, T_{c1} = 380 K, T_2 = 355 K)	6			55
$C_6H_5N(CH_3)_3CdBr_{3x}Cl_{3(1-x)}$	1D			***mm2Fm*** (Ama_2-Cc, T_c = 453 K)	2	3.6	0.215	20
R-LIPF ([(*R*)-1-(4-chlorophenyl)ethylammonium]$_2PbI_4$)	2D		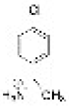	**422F1** ($P422$-$P1$, T_c = 483 K)	8	13.96		56

View Article Online
DOI: 10.1039/D5SC10231F

S-LIPF ([(*S*)-1-(4-chlorophenyl)ethylammonium]$_2$PbI$_4$)	2D	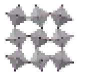	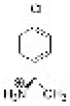	**422F1** (*P*422-*P*1, T_c = 473.2 K)	8	13.96	56
[(*R*)-PEDA]PbI$_4$ (PEDA^{2+} = *N*-(1-phenylethyl)ethane-1,2-diaminium)	2D		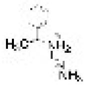	**222F2** ($P2_12_12_1$-$P2_1$, T_c = 389 K)	2	0.15	57
[(*S*)-PEDA]PbI$_4$	2D	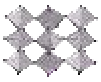		**222F2** ($P2_12_12_1$-$P2_1$, T_c = 389 K)	2	0.15	57
MFP ([cyclohexanemethylaminium]$_2$PbCl$_4$)	2D	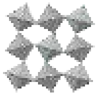		$\mathbf{4/mmmFmm2}$, $\mathbf{\bar{4}2mFmm2}$ (*I*4/*mmm*-γ-*Pmc*2$_1$-*Cmc*2$_1$, T_{c1} = 413.2 K, T_{c2} = 411.8 K, T_3 = 316.2 K)	2, 2	15.4 (300 K) 5.4 (316 K)	48
((*S*-3FQ)$_4$RbEu(NO$_3$)$_8$ *S*-3FQ$^+$ = (*S*)-3-fluoroquinuclidinium)	2D	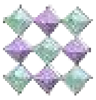		**4F1** ($P4_2$-*P*1, T_c = 441 K)	4	1.5	58
(*R*-3AP)RbBr$_3$ (*R*-3AP^{2+}= (*R*)-3-ammoniopyrrolidinium)	3D	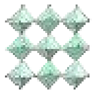		**432F2(*s*)** (*P*432-$P2_1$, T_c = 401 K)	12	1.21	34
(*R*-M3HQ)$_2$ RbLa(NO$_3$)$_6$ (*R*-M3HQ$^+$ = (*R*)-*N*-methyl-3-hydroxyl-quinuclidinium)	3D	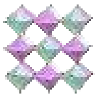	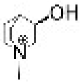	**23F3** ($P2_13$-*R*3, T_c = 278 K)	4	0.32	19
(*R*-M3HQ)$_2$NH$_4$ La(NO$_3$)$_6$	3D	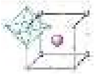	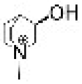	**23F3** ($P2_13$-*R*3, T_c = 314 K)	4		19
(*R*-M3HQ)$_2$ RbEu(NO$_3$)$_6$	3D	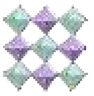		**23F3** ($P2_13$-*R*3, T_c = 285 K)	4	0.38	26
(*S*-M3HQ)$_2$ RbEu(NO$_3$)$_6$	3D	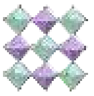		**23F3** ($P2_13$-*R*3, T_c = 284 K)	4		26
(*R*-M3HQ)$_2$ RbPr(NO$_3$)$_6$	3D	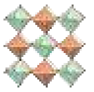	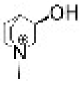	**23F3** ($P2_13$-*R*3, T_c = 280 K)	4	0.32	59
MHyZn ([CH$_3$NH$_2$NH$_2$]Zn(HCOO)$_3$)	3D	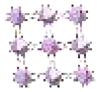	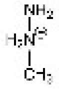	$\mathbf{\bar{3}mF3m, 3mF1}$ （$R\bar{3}c$-$R3c$-*P*1, T_{c1} = 321 K, T_{c2} = 178 K)	1, 6	3	60
(*R*-3HP)$_2$RbBiBr$_6$ (*R*-3HP$^+$ = (*R*)-3-hydroxypyrrolidinium)	3D	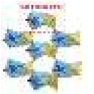		**2F1** ($P2_1$-*P*1, T_c = 394 K)	2	1.94 (b-axis) 3.18 (c-axis)	61
R-3-FPC	3D			**222F2** ($C222_1$-$P2_1$, T_c = 430 K)	2	9.4	62

View Article Online
DOI: 10.1039/D5SC10231F

([(*R*)-3-fluoropyrrolidinium]$_2$[KFe(CN)$_6$])						
S-3-FPC ([(*S*)-3-fluoropyrrolidinium]$_2$[KFe(CN)$_6$]	3D			**222F2** ($C222_1$-$P2_1$, T_c = 428 K)	2	62

4. Molecular multiferroics with ferroelectricity and ferroelasticity

The single-phase molecular multiferroic materials with ferroelectricity and ferroelasticity described in this review, including single molecules, perovskite structural hybrids and non-perovskite structural compounds, are summarized in Table 1. In addition, compounds that conform to one of the 42 species of full ferroelectric and full ferroelastic phase transitions defined by Aizu, but have not been characterized or investigated for ferroelasticity by the original authors and are listed in Table S1.

4.1 Single-component molecular multiferroics

Guided by Aizu's group-to-subgroup principle, 42 species of materials are known to exhibit coexisting ferroelectric and ferroelastic phase transitions, with 17 of these involving transitions from a chiral group to a chiral subgroup. This highlights the efficacy of introducing crystallographic chirality via homochiral organic cations as a strategic approach for designing molecular multiferroics. Moreover, molecular homochirality imparts these materials with unique and attractive physical attributes, such as circularly polarized luminescence (CPL), chiroptical nonlinear optical effects, chiral-induced spin selectivity and CPL detection making them highly relevant for advanced optoelectronic and spintronic applications. For example, Xiong group[49] introduces an organosilicon component of -$Si(CH(CH_3)_2)_2$ as a ligand into axial-chiral 1,1′-bi-2-naphthol (BINOL) to construct a pair of enantiomeric molecular multiferroics, (*R*)-BINOL-DIPASi and (*S*)-BINOL-DIPASi, which ingeniously combines the intrinsic polar and axial chirality of BINOL with a dynamic organosilicon component as displayed in Fig.4a. Structural characterization via SC-XRD confirmed that (*R*)-BINOL-DIPASi and (*S*)-BINOL-DIPASi exhibit a 2F1-type full ferroelectric and full ferroelastic phase transition at 362 K and 363 K, respectively. This transition is attributed to the order-disorder dynamics of the isopropyl groups within the organosilicon ligands. Electrical measurements, specifically *P-E* hysteresis loops, indicated spontaneous polarizations (P_s) of approximately 1.6 and 1.7 $\mu C \cdot cm^{-2}$. Furthermore, PFM directly visualized ferroic domain switching induced by a 110 V electric field, while PLM provided insights into the temperature-driven evolution of stripe-shaped ferroelastic domains. Nanoindentation measurements further reveal favorable mechanical softness (elastic modulus ~7 GPa). This work demonstrates the exceptional efficacy of axial chirality in constructing high-temperature single-component molecular multiferroics with good flexibility.

Integrating metal elements with organic components can also give rise to multifunctional coordination compounds. Recently, Ai et al. [41] reports the molecular multiferroic crystal $Fe^{II}(C_8\text{-F-pbh})_2$ (C_8-F-pbh = (1*Z*,*N*′*E*)-3-F-4-(octyloxy)-*N*′-(pyridin-2-ylmethylene)benzohydrazonate), as shown in Fig.4b, demonstrating the coexistence of ferroelectricity, ferroelasticity and spin-crossover (SCO) behavior within a single phase, representing a significant breakthrough integrating multiple order parameters. By the H/F substitution, the T_c of $Fe^{II}(C_8\text{-F-pbh})_2$ (318 K) is much higher than that of the non-fluorinated parent compound (270 K), which enabling it room-temperature functionality. Structural analysis reveals that the phase transition, driven by the 180° flip-flop motion of partial fluorobenzene moiety and the ordering of flexible alkyl chains, corresponds to a symmetry breaking from the paraferroic phase (space group $P2_12_12_1$) to the ferroic phase (space group $P2_1$), which is classified as the 222F2-type full ferroelectric and full ferroelastic phase transition. The reversible switching of ferroelectric and ferroelastic domains with temperature is directly visualized via PFM and PLM in Fig. 3, respectively. Besides, $Fe^{II}(C_8\text{-F-pbh})_2$ displays a spin transition between high- and low-spin states, accompanied by the *d*-orbital breaking within the $t_{2g}^4e_g^2$ and $t_{2g}^6e_g^0$ configuration change of octahedrally coordinated Fe^{II} center as shown in Fig.4b. This finding would further inspire the exploration of multiple-state molecular switches.

4.2 Organic-inorganic hybrid multiferroics with ferroelectricity and ferroelasticity

4.2.1 Organic-inorganic hybrid perovskites (OIHPs)

Organic-inorganic hybrid perovskites (OIHPs) have attracted much attention in recent years because of their diverse structures and rich physical properties, including zero-dimensional (0D) isolated structures, one-dimensional (1D) chain-like, two-dimensional (2D) layered, and three-dimensional (3D) cage-like configuration. They also reveal a wide range of component variations, such as organic hybrid metal halides, formate-bridged ligands, and double perovskite structures (*e.g.*, monovalent alkali metal or ammonium ions paired with trivalent rare-earth metals). The recent progress in single-phase molecular multiferroics based on different perovskite structure types are reviewed according to their dimensional classification.

Zero-dimensional Organic-inorganic hybrid perovskites (0D OIHPs)

Introducing homochirality into molecular ferroelectrics provides an effective route to realize chiral ferroelectric functionalities. In 2025, Liao et al.[52] reported a pair of molecular ferroelectric enantiomerics, [RFAO][ReO_4] and [SFAO][ReO_4] (RFAO/SFAO = (4*R*,5*R*)/(4*S*,5*S*)-4-fluoro-1-azabicyclo[3.2.1]octane). This pair of ferroelectric enantiomers crystallize in the chiral–polar point group 2 at room temperature and undergo two successive ferroelectric phase

View Article Online
DOI: 10.1039/D5SC10231F

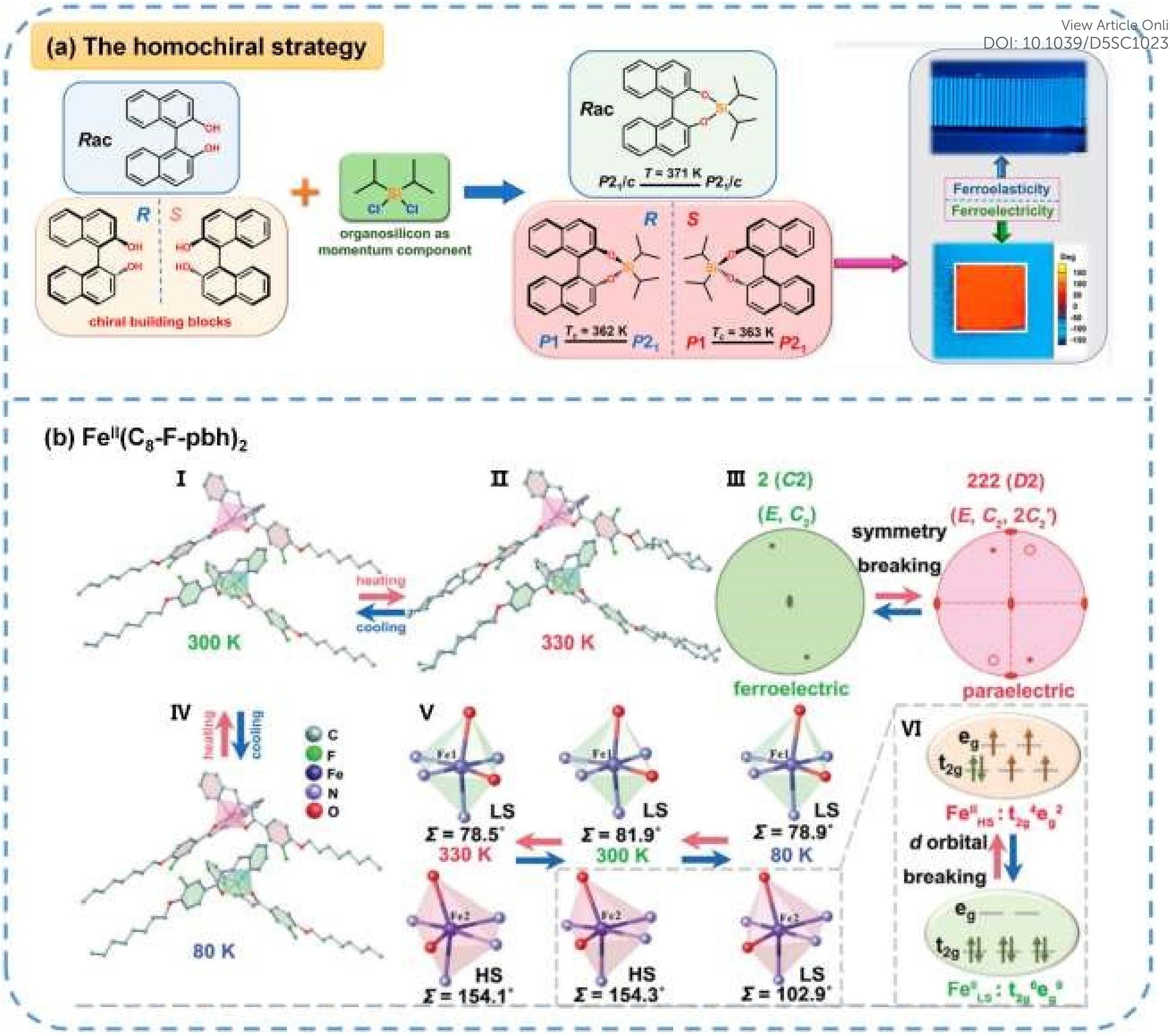

Fig.4 (a) Design concept of (*R*)-BINOL–DIPASi and (*S*)-BINOL–DIPASi as single-component molecular multiferroic crystals. The stripe-shaped ferroelastic domains and rectangular ferroelectric domains of (*R*)-BINOL–DIPASi are imaged by PLM and PFM, respectively. (b) The crystallographic structure, symmetry and SOC of $Fe^{II}(C_8\text{-F-pbh})_2$: The structure at 300 K (I), 330 K (II) and 80 K (IV). (III) Equatorial plane projection of the point group of *C*2 in the ferroelectric phase and D2 in the paraelectric phase, showing symmetry breaking. (V) Enlarged octahedrons of $Fe^{II}N_4O_2$ coordination sphere in the different phases, showing LS/HS states. (VI) Electronic structures of the Fe^{II} HS/LS states, showing *d* orbital breaking. Reproduced from ref. 49 and 41 with permission from American Chemical Society and Wiley, Copyright 2022 and 2024.

transitions with Aizu notations of 222F2 at 350 K and 432F2 at 463 K, respectively. The symmetry evolution from 2 to 222 and then to 432 is associated with the order–disorder behavior of the organic cations and anions within the crystal lattice. As a result, the enantiomeric crystals exhibit switchable spontaneous polarization together with a multistep second-harmonic generation circular dichroism (SHG-CD) response from high to low and finally to inactive states. More importantly, spiral chiral ferroelectric domains were directly observed in the enantiomeric crystals, representing the first discovery of chiral domain configurations in enantiomeric ferroelectric materials and highlighting the intrinsic coupling between polarization and chirality.

One-dimensional Organic-inorganic hybrid perovskites (1D OIHPs)

Introduction homochirality into 1D chain-like OIHPs (ABX_3, where A = organic cation, B = divalent metal ion, X = halogen) also serves as an effective strategy for constructing ferroelastic–ferroelectric multiferroics. In 2022, Fu et.al[55] found the first 1D homochiral hybrid perovskite [(*R*)-*N*-ethyl-3-quinuclidinol]PbI_3 ([*R*-EQ]PbI_3) with the coexistence of full ferroelectricity and full ferroelasticity. At 380 K, [*R*-EQ]PbI_3 undergoes a phase transition with the Aizu notation of 622F2(*s*), as shown in Fig.5a and reveals a multiaxial ferroicity (the six equivalent coupling polarization and strain orientations) at room temperature. Nevertheless, both racemic analogue [*Rac*-EQ]PbI_3 and the achiral parent compound [EQ]PbI_3 (EQ = *N*-ethyl-quinuclidine) only experience the paraferroelastic-ferroelastic phase transition

View Article Online
DOI: 10.1039/D5SC10231F

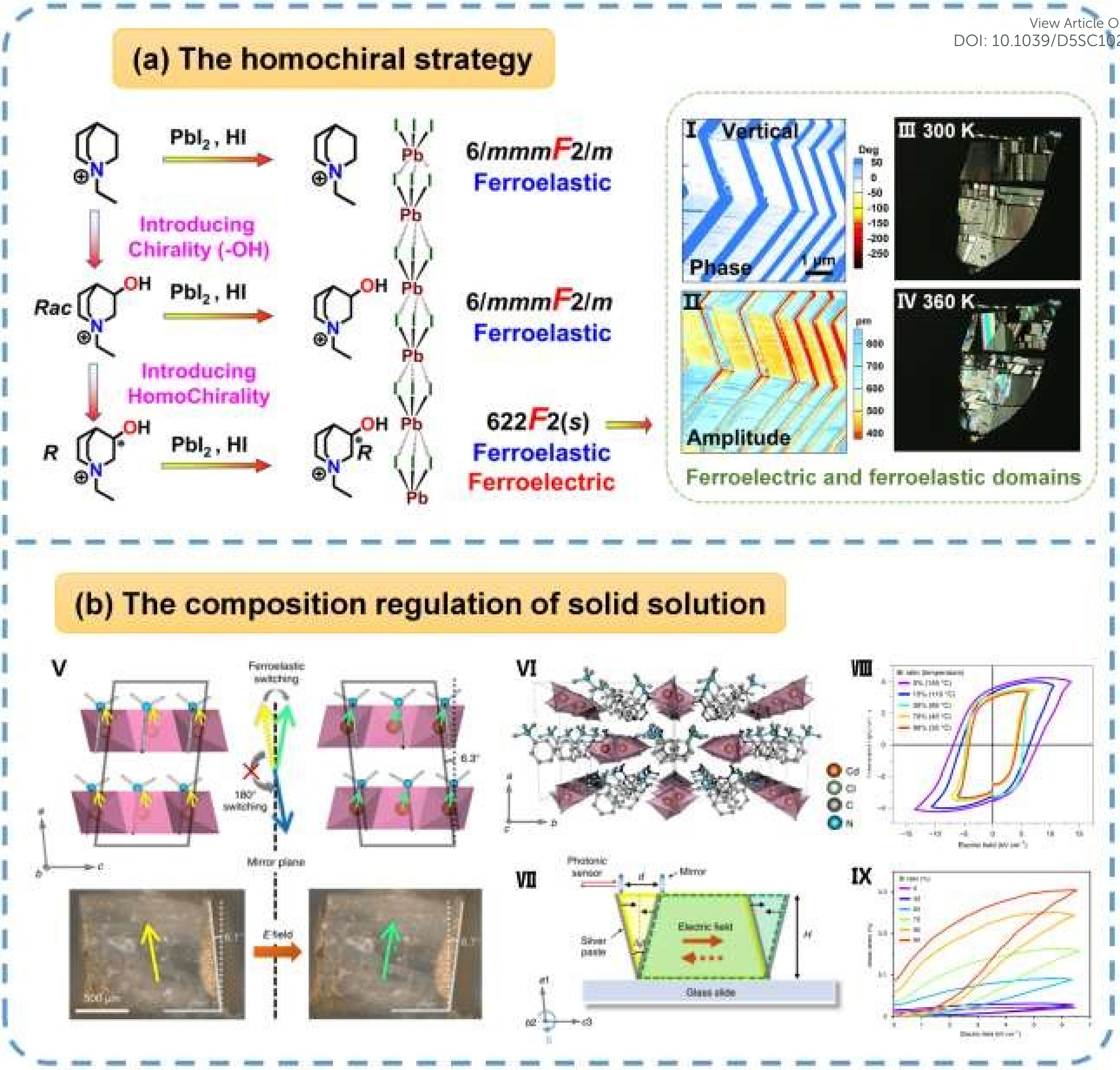

Fig.5 (a) Design of 1D multiferroic[*R*-EQ]PbI$_3$ through introducing homochirality. Its stripe-shaped ferroic domains are imaged by PFM (I, II) and PLM (III, IV), respectively. (b) Top: illustration of structural units of C$_6$H$_5$N(CH$_3$)$_3$CdBr$_{3x}$Cl$_{3(1-x)}$ in the two ferroelastic states and structure confinement effect for ferroelectric/ferroelastic switching. (V) The yellow and green arrows indicate the polarization directions. Bottom: photos of a bulk single crystal poled to the two ferroelastic states by the electric field, showing a macroscopic shear strain in good correlation with the unit cell distortion. (VI) Perspective of crystallographic structure along the 1D chain direction. (VII) Experimental setup for the shear strain and piezoelectricity measurements. (VIII) *P-E* loops of the solid solution series at a measurement frequency of 2 Hz. (IX) Unipolar *S*–*E* curves of the solid solution series at 2 Hz after pre-poling. Reproduced from ref. 55 and 20 with permission from American Chemical Society and Springer Nature, Copyright 2022 and 2021.

with the same Aizu notation of 6/*mmm*F2/*m*, and they possess the six equivalent strain orientations in their ferroelastic phase.

Researchers have long theorized that full ferroelectric and full ferroelastic coupling could induce the large deformation of material, thereby generating giant piezoelectric responses. Significant experimental breakthroughs in this area remained elusive until Hu et al.[20] achieved them through halogen doping of the inorganic framework. Their investigation into a series of 1D solid-solution crystals, exemplified by C$_6$H$_5$N(CH$_3$)$_3$CdBr$_3$Cl$_{3(1-x)}$ (Fig. 5b), revealed unprecedented electromechanical performance. Specifically, applying an electric field after electrode deposition on opposing faces of C$_6$H$_5$N(CH$_3$)$_3$CdCl$_3$ single crystals resulted in a substantial shear strain of up to 21.5%, a magnitude two orders higher than that found in conventional ferroelectric polymers and oxides. This exceptional performance is achieved through inorganic bond switching and enhanced by the structural confinement provided by large organic moieties, which effectively suppresses undesired 180° polarization switching. Furthermore, Br substitution in the hybrid ferroelectric C$_6$H$_5$N(CH$_3$)$_3$CdCl$_3$ was employed to systematically tune phase transition temperatures, and mechanical properties, and

View Article Online
DOI: 10.1039/D5SC10334F

piezoelectricity. Notably, in the Br-rich end of the solid solution, the sizable shear piezoelectric coefficient (d_{35}) is up to 4830 pm V^{-1}.

Two-dimensional Organic-inorganic hybrid perovskites (2D OIHPs)

Introducing homochirality into 2D OIHPs ($A^{I}_2BX_4$/$A^{II}BX_4$-type structure) in 2019, Xiong group[56] designed and synthesized the first pair of 2D lead-iodide perovskite enantiomerics, [*R*- and *S*-1-(4-chlorophenyl)ethylammonium]$_2$PbI$_4$ (*R*- and *S*-LIPF) in Fig.6a, which show full ferroelectricity and full ferroelasticity at room temperature, whereas their racemic analogue [*Rac*-1-(4-chlorophenyl)ethylammonium]$_2$PbI$_4$ adopts a centrosymmetric space group *P*2$_1$/*c*. Notably, *R*-LIPF and *S*-LIPF undergo the ferroic phase transitions described by the Aizu notation of 422F1, and their transition temperature as high as 483 and 473.2 K, respectively. Using PLM, the reversible disappearance and reappearance of their ferroelastic domains across the phase transition were clearly visualized. Furthermore, PFM measurements confirm that their ferroelectric domains can be switched under an applied electric field, directly verifying their multiferroic nature. Additionally, bothenantiomers possess semiconductor characteristics with a direct bandgap of 2.34 eV. Based on the homochiral strategy, Zeng et al.[57] in 2021 achieved a further breakthrough by designing [(*R*)- and (*S*)-*N*-(1-phenylethyl)ethane-1,2-diaminium]PbI$_4$ ([(*R*)- and (*S*)-PEDA]PbI$_4$). They not only displays a 222F2-type ferroelectric phase transition at ~389 K but also demonstrates coupled ferroelastic domain switching and reversible thermochromism, and the crystals of [(*R*)- and (*S*)-PEDA]PbI$_4$ manifest the color change from orange-yellow to orange-red driven the temperature. This study represents the first integration of ferroelectricity, ferroelasticity, and

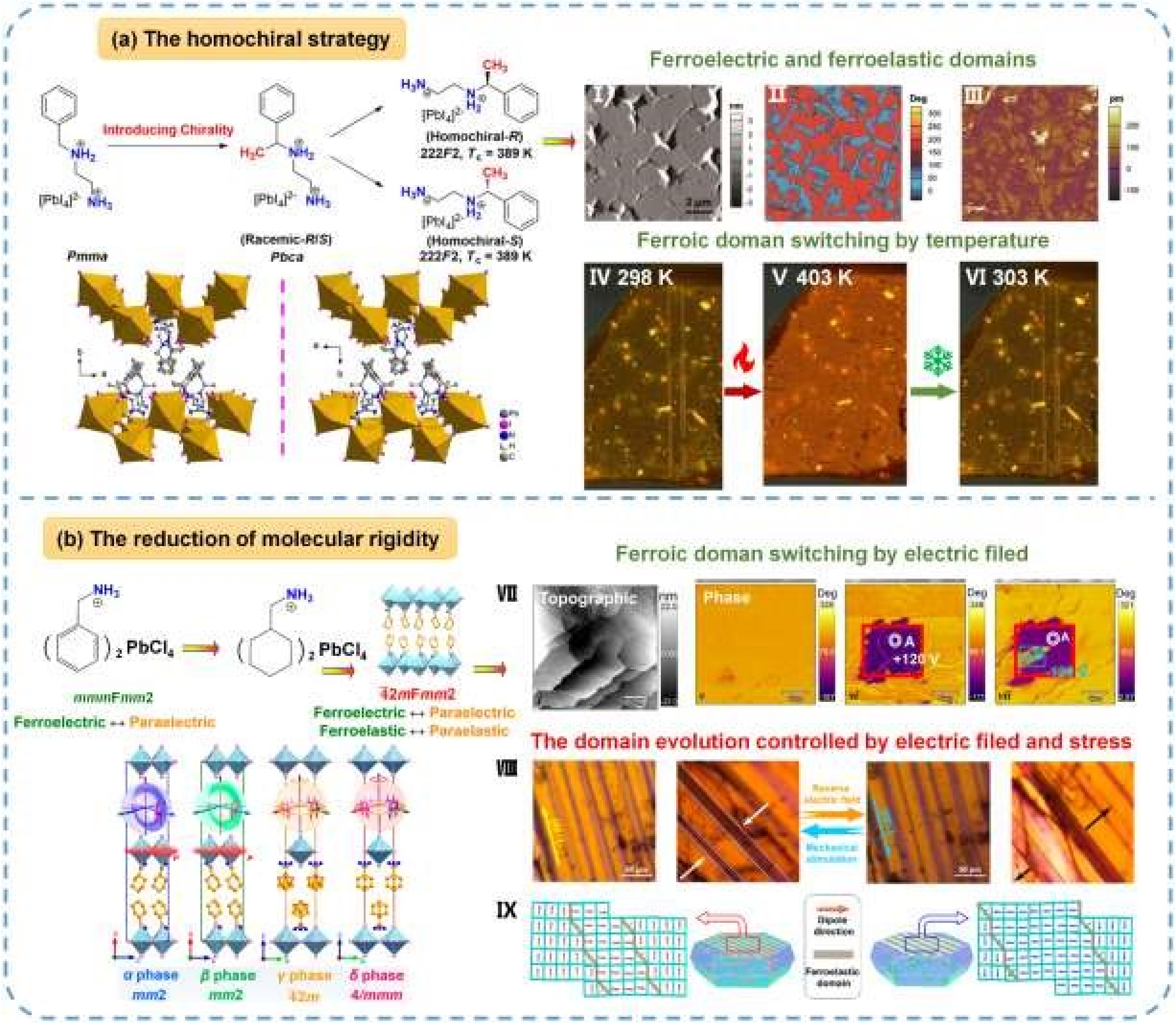

Fig.6 (a) The approach of molecular design for the 2D homochiral perovskite multiferroic. Packing views of the crystal structures of *R*-LIPF (left lower) and *S*-LIPF (right lower). (I) The topographic image, vertical PFM phase (II) and amplitude (III) images of *R*-LIPF thin film. Ferroelastic domain evolution of 1-R in the continuous heating and cooling process at 298 K (IV), 423 K (V), and 303 K (VI). (b) Design of 2D multiferroic MFP through reducing molecular rigidity and packing views of MFP at different phases. Inset: stereosymmetric operation matching with the crystal lattice. (VII) Morphology, amplitude, and phase images for the 20 × 20 µm region, which are observed in the as-grown state and observed after applying a voltage of +120 V in the red rectangle wireframe and subsequently −120 V in the blue rectangle wireframe. (VIII) Observation of ferroelastic domain evolution controlled by electric and mechanical fields under a polarizing microscope. (IX) Schematic diagram of the evolution of ferroelastic domains under electric and stress fields. Reproduced from ref. [57] and [48] with permission from Wiley and American Chemical Society, Copyright 2021 and 2024.

View Article Online
DOI: 10.1039/D5SC10231E

thermochromism in a single chiral perovskite, underscoring the versatility of molecular level chirality engineering for creating multifunctional OIHPs. However, none of the aforementioned studies have performed the coupling characterization between ferroelectric polarization and ferroelastic strain in multiferroic OIHPs, such as observing electric-field-controlled ferroelastic domain switching via PLM or stress-modulated ferroelectric domain switching via PFM.

Since the concept of multiferroicity was introduced in 1968, the coupled effect of polarization and strain in full ferroelectricity and full ferroelastic had never been experimentally observed in OIHPs. Until 2024, our group reported a 2D multiferroic hybrid perovskite (cyclohexanemethylaminium)$_2$PbCl$_4$ (MFP) with full ferroelectricity and full ferroelasticity as displayed in Fig.6b.[48] This study demonstrates that MFP undergoes a symmetry-breaking transition of $\bar{4}2m$F$mm2$ type at 411.8 K, driven by dynamic reorientations of flexible organic cations. MFP exhibits a large spontaneous polarization of 15.4 μC·cm^{-2} at room temperature, whereas its rigid structural parent compound merely shows ferroelectricity. Importantly, the in-situ switchable evolution of ferroelastic domains under either electric or mechanical fields is directly observed, representing the first experimental demonstration of coupled polarization-strain orientation-switching dynamics in hybrid perovskites.

Three-dimensional Organic-inorganic hybrid perovskites (3D OIHPs)

The 3D OIHPs (ABX$_3$-type structure) are constrained by Goldschmidt's tolerance factor, and the multiferroicity in such structure is also rarely reported so far. Zhang and colleagues[34] introduced a homochiral organic cation, (*R*)-3-ammoniopyrrolidinium (*R*-3AP) in Fig.7a, into a rubidium-bromide framework, gaining multiferroic (*R*-3AP)RbBr$_3$. (*R*-3AP)RbBr$_3$ undergoes a reversible ferroelectric–ferroelastic phase transition at 401 K, identified by the Aizu notation 432F2(*s*). This transition is driven by the order-disorder transition of organic cations and Jahn-Teller distortion of the inorganic framework. (*R*-3AP)RbBr$_3$ clearly exhibits multiferroicity, evidenced by a saturation polarization of 1.21 μC·cm^{-2}, a reversible second harmonic generation switch, and observable, reversible ferroelastic domain evolution when viewed under a polarizing microscope.

4.2.2 The 3D metal–organic frameworks (MOFs)

In addition to 3D perovskite structure of organic hybrid metal halides, there exists a category of compounds with the general formula ABX$_3$ (A = protonated amine, B = metal cation and X = HCOO$^-$) metal-organic frameworks (MOFs), in which formate (OCO$^-$) anions replace halides as bridging ligands. Such frameworks can generally accommodate larger organic cations compared to their halide-based counterparts. Sieradzki group[60] found [CH$_3$NH$_2$NH$_2$][Zn(HCOO)$_3$] (MHyZn) as illustrated in Fig.7b, which adopts the typical AMX$_3$ structure where the anionic [Zn(HCOO)$_3$]$^-$ framework creates cube-like cavities hosting the polar methylhydrazinium (MHy$^+$) cations, interconnected via hydrogen bonds and Coulomb interactions. MHyZn exhibits two distinct structural phase transitions: a high-temperature improper ferroelectric transition from a centrosymmetric paraelectric phase ($R\bar{3}c$) to a polar phase ($R3c$) around 321 K, and a low-temperature

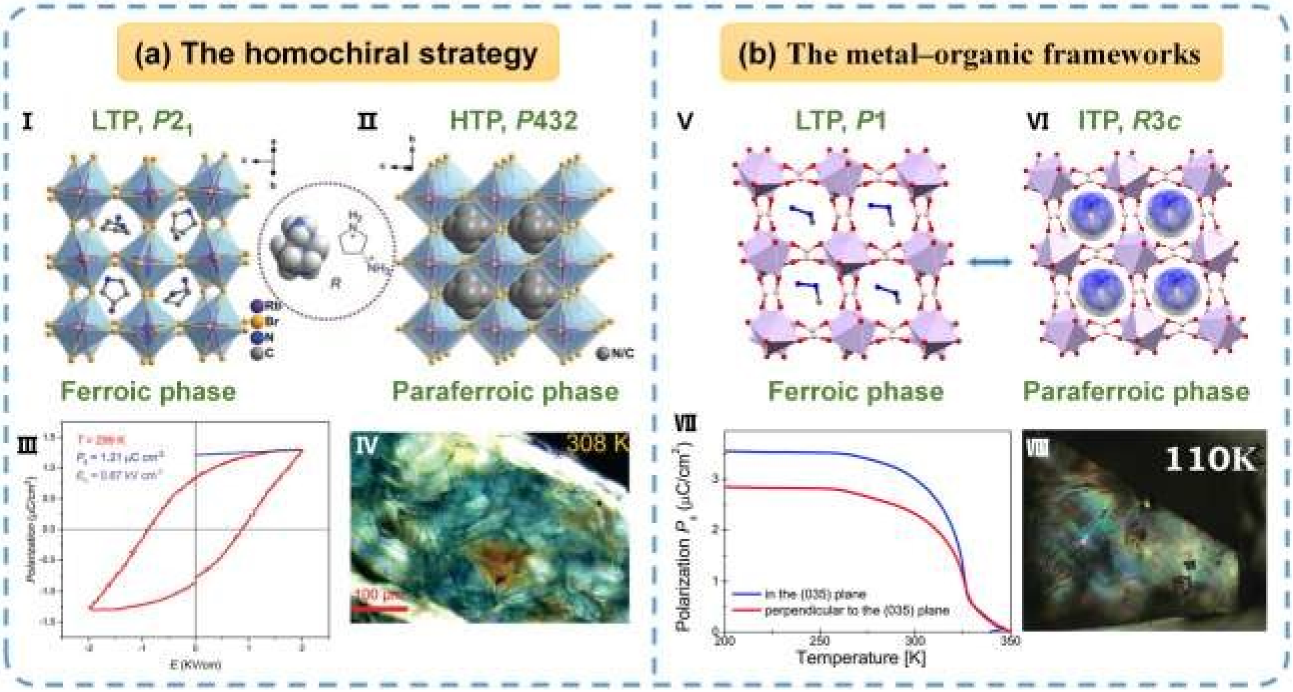

Fig.7 (a) The 3D multiferroic (*R*-3AP)RbBr$_3$: Packing views of (*R*-3AP)RbBr$_3$ in ferroic (I) and paraferroic phase (II). (III) Its *P-E* hysteresis loop measured by Sawyer-Tower method at 299 K. (IV) The domain structure of (*R*-3AP)RbBr$_3$ at 308 K. (b) The 3D metal-organic framework MHyZn: Packing views of MHyZn in ferroic (V) and paraferroic phase (VI). (VII) The spontaneous polarization of MHyZn determined from the temperature dependent pyroelectric current measurements. (VIII) The stripe-shaped ferroic domains of MHyZn at 110 K. Reproduced from ref. 34 and 60 with permission from Wiley and The Royal Society of Chemistry, Copyright 2024 and 2018.

View Article Online
DOI: 10.1039/D5SC10231F

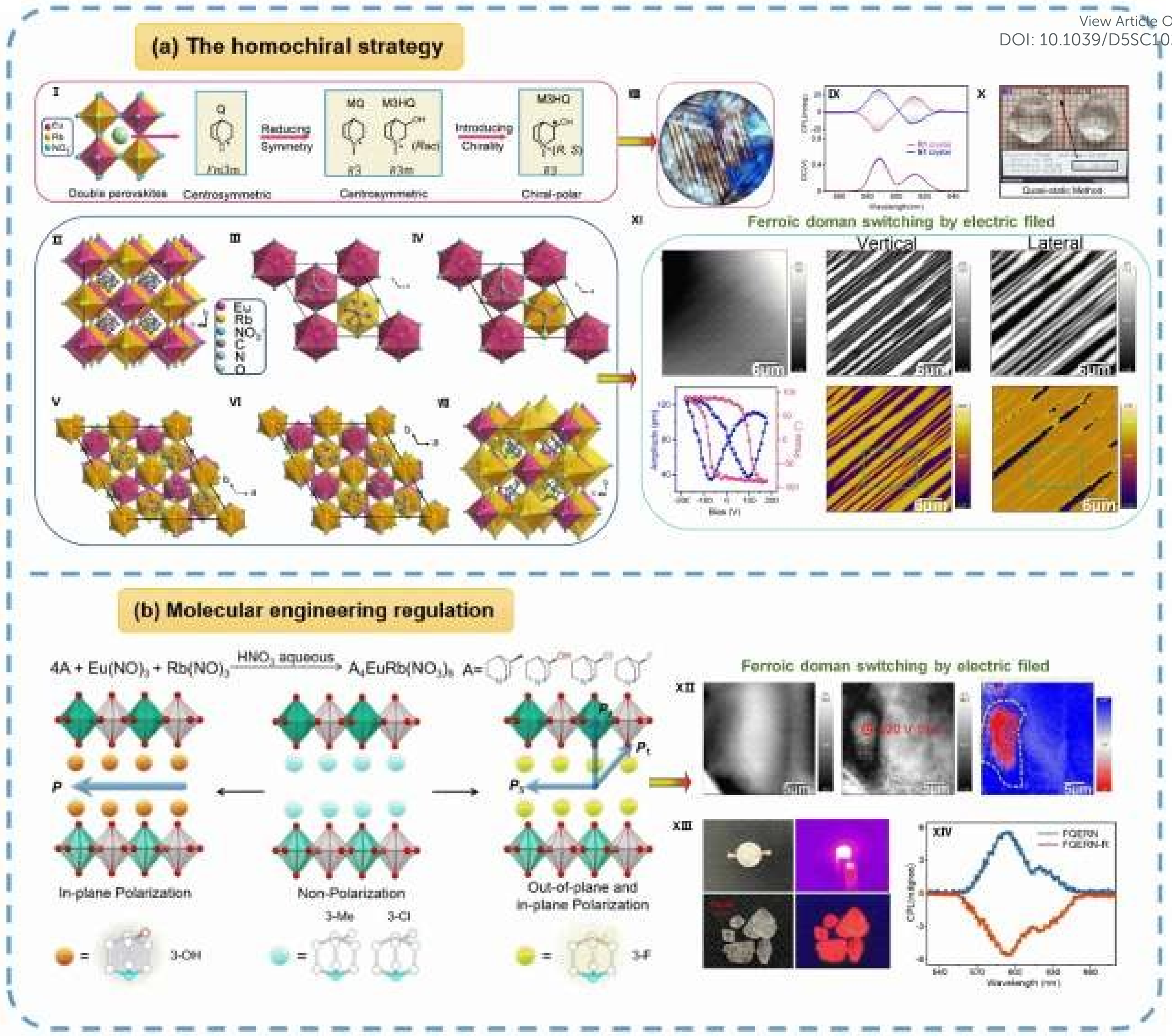

Fig.8 (a) The 3D nitrate-bridged rare-earth double perovskites (*R*- and *S*-M3HQ)$_2$RbEu(NO$_3$)$_6$: (I) Design strategy and crystal structures of these perovskites. (II) (Q)$_2$RbEu(NO$_3$)$_6$ at 293 K. (III) (MeQ)$_2$RbEu(NO$_3$)$_6$ at 293 K. (IV) *Rac* at 293 K. (V) (*S*-M3HQ)$_2$RbEu(NO$_3$)$_6$ at 253 K. (*R*-M3HQ)$_2$RbEu(NO$_3$)$_6$ at 253(VI) and 303 (VII) K. The NO$_3^-$ ions are simplified as balls for clarity. (VIII). (b) Molecular engineering regulation achieving multipolar axes and out-of-plane polarization in rare-earth hybrid double perovskite ferroelectric. (XII) PFM topography, amplitude, and phase images after the first electric poling with tip-bias of -220 V. (XIII) Single-crystal blocks and red LED packaged with a 365 nm chip under daylight and ultraviolet light. (XIV) CPL spectra excited by 396 nm. Reproduced from ref. 58 and 26 with permission from Wiley and The Royal Society of Chemistry, Copyright 2024 and 2022.

ferroelectric and ferroelastic transition to a triclinic phase (*P*1) near 178 K, corresponding to the Aizu notation 3*m*F1. Structural analysis indicates that both transitions are driven by temperature-induced order–disorder transformations of the MHy$^+$ organic cations. However, the coexistence of full ferroelectric and ferroelastic orders in MHyZn occurs well below room temperature, significantly limiting its practical applicability. Clearly, careful selection of organic cations can yield new multiferroic formates, but the number of such compounds remains limited thus far.

4.2.3 The nitrate-bridged rare-earth double perovskites

Double-metal perovskites represent an important subclass of OIHPs, distinguished by their capacity to combine diverse metals and oxidation states. This unique feature enables them to exhibit a range of intriguing chemical and physical properties often unattainable in organic hybrid single-metal halide perovskites. A significant category comprises nitrate-bridged rare-earth double perovskites, exemplified by structures like 2D A$_4$B$_1$^{I}B$_2$^{III}(NO$_3$)$_8$ and 3D A$_2$B$_1$^{I}B$_2$^{III}(NO$_3$)$_6$ (Fig.8a and Fig.8b).[63] Rare-earth double perovskites distinguish themselves from traditional organic–inorganic hybrid perovskites by offering a higher structural tunability, because there is much room for tailoring the structure by varying the organic cation, the alkaline metal ion, and the rare-earth ion. Meanwhile, by introducing the unique electronic structures of rare-earth ions, these materials have great potential in the multifunctional coupling of photoluminescence, magnetism, ferroelasticity and ferroelectricity. Notably, the Zhang group has pioneered the research of such materials by incorporating homochiral organic cations (*R*- and *S*-

View Article Online
DOI: 10.1039/D5SC10031F

M3HQ = (*R*)- and (*S*)-*N*-methyl-3-hydroxylquinuclidinium), successfully creating a series of rare-earth double perovskites that exhibit coexisting ferroelectricity and ferroelasticity. For instance, in 2020, the first multiferroic compound in this family, (*R*-M3HQ)$_2$RbLa(NO$_3$)$_6$, was reported.[19] It undergoes a relaxor-type full ferroelectric and full ferroelastic phase transition with the Aizu notation 23F3 at 278 K. Of note, it exhibits a large piezoelectric coefficient d_{33} of 106 pC • N^{-1}, resulting from polar microdomains existing in nonpolar regions, and these polar microdomains lead to the easy polarization rotation of the polar microdomains upon applying a stress. This work confirmed that the coupling the ferroelectricity and ferroelasticity allows rotating the polarization by applying a stress, and highlighting such coupling as an effective strategy for achieving superior piezoelectric performance.

Subsequently, by replacing the rare-earth ion with Eu^{3+} and Pr^{3+}, a pair of enantiomeric compounds (*R*- and *S*-M3HQ)$_2$RbEu(NO$_3$)$_6$, as well as (*R*-M3HQ)$_2$RbPr(NO$_3$)$_6$, are synthesized.[26] These derivatives maintain the same Aizu phase transition type and similar transition temperatures as the parent compound (*R*-M3HQ)$_2$RbLa(NO$_3$)$_6$, while exhibiting comparable piezoelectric coefficients (d$_{33}$ ≈ 103 and 102 pC • N^{-1}, respectively). Notably, (*R*- and *S*-M3HQ)$_2$RbEu(NO$_3$)$_6$ simultaneously achieve CPL and piezoelectric response, demonstrating the coupling between optical activity and ferroic order states as shown in Fig.8a. The most recent work introduced fluorine substitution on the organic cation to gain the 2D (*S*-3FQ)$_4$EuRb(NO$_3$)$_8$ (*S*-3FQ=(*S*)-3-fluoroquinuclidinium) in Fig.8b, which undergoes a full ferroelectric and full ferroelastic phase transition with the Aizu nation of 4F1 at the 411 K.[59] (*S*-3FQ)$_4$EuRb(NO$_3$)$_8$ successfully engineers out-of-plane polarization and elevates the Curie temperature by 94 K compare to the (*S*-3HQ)$_4$EuRb(NO$_3$)$_8$ (*S*-3HQ = (*S*)-3-hydroxylquinuclidinium) , and retaining CPL activity in a two-dimensional rare-earth double perovskite. Since there is much room for tailoring the structure by varying the organic cation, the alkaline metal ion, and the rare-earth ion, this series of work will lead to discovery of novel rare-earth-based materials with excellent ferroelectricity, piezoelectricity, and other optoelectronic properties.

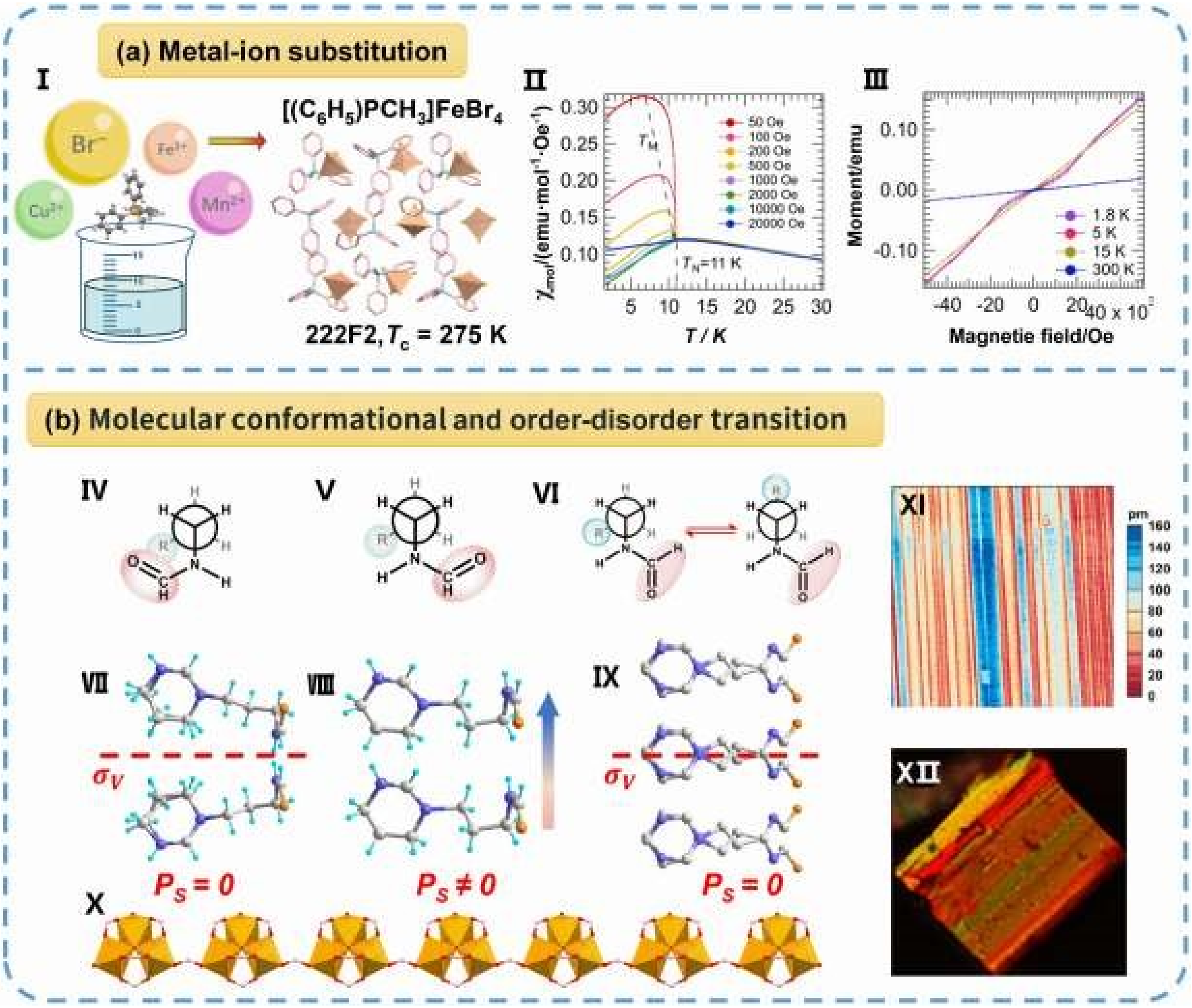

Fig. 9 (a) Design of 0D multiferroic [(C$_6$H$_5$)$_3$PCH$_3$]FeBr$_4$ through substituting metal-ion (I). (II) Zoomed in result for [(C$_6$H$_5$)$_3$PCH$_3$]FeBr$_4$ susceptibility. (III) Zoomed in magnetization of compound with respect to applied field at different temperature. (b) The 1D trinuclear iron–oxo anionic chain complex [FPM][Fe$_3$(μ$_3$-O)(μ-O$_2$CH)$_8$]: The Newman projection and packing views of the FPM cation at LTP (IV,VII), ITP (V, VIII), and HTP (VI, IX). The "*R*" group stands for −CH$_2$−C$_4$H$_8$N$_2$. (X)The trinuclear iron–oxo anionic chain at 250 K. PFM amplitude (XI) and

View Article Online
DOI: 10.1039/D5SC10231F

ferroelastic domain patterns (XII) of [FPM][$Fe_3(\mu_3\text{-}O)(\mu\text{-}O_2CH)_8$]. Reproduced from ref. 50 and 54 with permission from Wiley and American Chemical Society, Copyright 2025 and 2024.

4.3 Non-perovskite structural multiferroics

The research progress on single-phase molecular multiferroics with non-perovskite structures is summarized here, including, 0D packing structures, 1D corner-sharing octahedral structure, 3D organic hybrid bimetal halide with lonsdaleite topology and cyanido-bridged dimetallic complexes.

0D non-perovskites

In 0D organic hybrid metal halides, organic cations and metal-halide frameworks are connected via the weak intermolecular interactions and electrostatic interactions, offering structural flexibility and strong compositional tunability. Numerous compounds with rich properties and promising applications have been reported. Due to the weak interactions between the organic and inorganic components, 0D hybrid metal halides can endure large ion displacements and reversible strain, which may lead to strong coupling between ferroelectricity and ferroelasticity. In 2021, Wu and colleagues[51] predicted via first-principles calculations that multiferroicity could emerge in 0D organic–inorganic hybrid halides as displayed in Fig.9a. By systematically substituting the metalcenters and halogen elements, researchers demonstrated that PH_4FeBr_4 exhibits a robust multiferroic coupling among ferroelectricity, ferroelasticity, and antiferromagnetism. This allows for the precise control of spin directions through either ferroelastic or 90° ferroelectric switching. Complementary simulation results further elucidated PH_4FeBr_4's potential, highlighting its ultra-low switching barrier and remarkable capacity to sustain large ion displacements and over 40% reversible strain. Unfortunately, the multiferroic behavior of PH_4FeBr_4 has not yet been experimentally verified. Most recently, Carpenter and co-workers[50] maintained the organic component $(C_6H_5)_3PCH_3^+$ constant while varying the metal centers (BBr_x, B = Fe^{3+}, Mn^{2+}, Cu^{2+}) and then discovered a new 0D organic–inorganic hybrid iron bromide, [$(C_6H_5)_3PCH_3$]$FeBr_4$, which simultaneously exhibits ferroelectricity, ferroelasticity, and antiferromagnetism below 11 K. Notably, [$(C_6H_5)_3PCH_3$]$FeBr_4$ undergoes a full ferroelectric and full ferroelastic phase transition at 275 K with the Aizu notation 222F2, driven by an order-disorder transition of the organic cations. Ferroelastic twinning in this compound has been confirmed by split reflections in a diffraction pattern collected at 100 K. However, the temperature at which multiferroicity coexists in this compound is far below room temperature, which limits its practical applicability. To the best of our knowledge, the number of reported 0D ferroelectric–ferroelastic multiferroic materials remains very limited.

1D non-perovskites

Compare to the aforementioned 1D OIHPs formed by face-sharing metal-halide octahedra, $(C_4H_8NH_2)_2[SbCl_5]$ adopts a 1D structure built from corner-sharing $[SbCl_5]^{2-}$ chains and pyrrolidinium cations.[53] Through comprehensive SC-XRD, dielectric spectroscopy, and ^1H NMR analysis, the authors elucidate three reversible structure transitions: from the high-temperature orthorhombic paraelectric phase I (space group *Pnmb*) down to the polar orthorhombic phases II (*Pmn*2_1), then to the polar monoclinic phases III (*Pn*), and IV (*P*2_1). The corresponding transition temperatures and Aizu notations are 252 K (*mmm*F*mm*2, ferroelectric phase transition), 247 K (*mm*2F*m*, full ferroelectric and full ferroelastic transition), 231 K (*m*F2, ferroelectric phase transition), respectively. These phase transitions induce ferroelectricity in II and III phases, with ferroelasticity observed in III and IV phases. It is noteworthy that III phase of $(C_4H_8NH_2)_2[SbCl_5]$ exhibits full ferroelectricity and full ferroelasticity according to the classification proposed by Aizu.[31] The underlying mechanism of these structure phase is attributed to a synergistic interplay between a "displacive" contribution from significant distortion of the inorganic $[SbCl_5]^{2-}$ chains and an "order-disorder" contribution arising from the progressive ordering and dynamic changes of the pyrrolidinium cations, stabilized by N-H⋯Cl hydrogen bonds. This work highlights the critical role of 1D polymeric anionic networks in promoting acentric crystal symmetries and provides valuable insights into the design of advanced hybrid ferroelectric materials.

Among 1D non-perovskite multiferroic compounds, the trinuclear iron–oxo anionic chain complex, [FPM][$Fe_3(\mu_3\text{-}O)(\mu\text{-}O_2CH)_8$] (where FPM is 3-(3-formylaminopropyl)-3,4,5,6-tetrahydropyrimidin-1-ium), serves as a compelling example.[54] As depicted in Fig.9b, this complex features organic counterions, formed by formamide groups acting as H-bond donors and acceptors linked to ammonium cations via alkyl chains, which impart significant conformational flexibility. This inherent conformational adaptability and the numerous H-bond binding sites within the FPM cation enable [FPM][$Fe_3(\mu_3\text{-}O)(\mu\text{-}O_2CH)_8$] to exhibit an unusual inverse temperature symmetry-breaking (ITSB) phase transition, alongside the coexistence of ferroelectricity and ferroelasticity, within the temperature range of 365-426 K. The ITSB is driven by a two-step process: an initial conformational flip of the flexible FPM counterions at 365 K (LTP to ITP, *Pca*2_1 to *Cc*), followed by a conventional order-disorder transition at 426 K (ITP to HTP, *Cc* to *Cmc*2_1). These sequential transitions are precisely described by the *mm*2F*m* species within the Aizu classification. Crucially, the coexistence of ferroelasticity and ferroelectricity was conclusively evidenced by comprehensive characterization using PLM and PFM. Importantly, the complex not only exhibits multistep ferroelectric and ferroelastic switching but also presents remarkable nonlinear optical switching properties, broadening its potential functionalities.

3D Organic hybrid bimetal halide with lonsdaleite topology

The report of $(R\text{-}3HP)_2RbBiBr_6$ (*R*-3HP = (*R*)-3-hydroxypyrrolidinium) in 2019, a landmark as the first 3D lead-free hybrid bimetal halide multiferroic featuring a lonsdaleite topology.[61] Its architecture is built upon mixed face- and corner-sharing connections between $[BiBr_6]^{3+}$ octahedra and $[RbBr_6O_2]^{9-}$ dodecahedra. These face-sharing linkages initially create bimetal dimers, which subsequently extend through corner-sharing to form a rigid 3D cage-like framework that effectively hosts the homochiral cations within its cavities (Fig.10a). At ambient temperature, this compound adopts the polar chiral space group P1, demonstrating coexisting ferroelectric and ferroelastic orders. A reversible phase transition occurs at approximately 394 K, marked by a symmetry breaking event consistent with the Aizu 2F1 species, primarily driven by the

View Article Online
DOI: 10.1039/D5SC10231F

reorientation of the chiral cations and the distortion of the bimetal anion framework Ferroelectricity of this compound is confirmed by *P-E* hysteresis loops, showing P_r of approximately 1.94 and

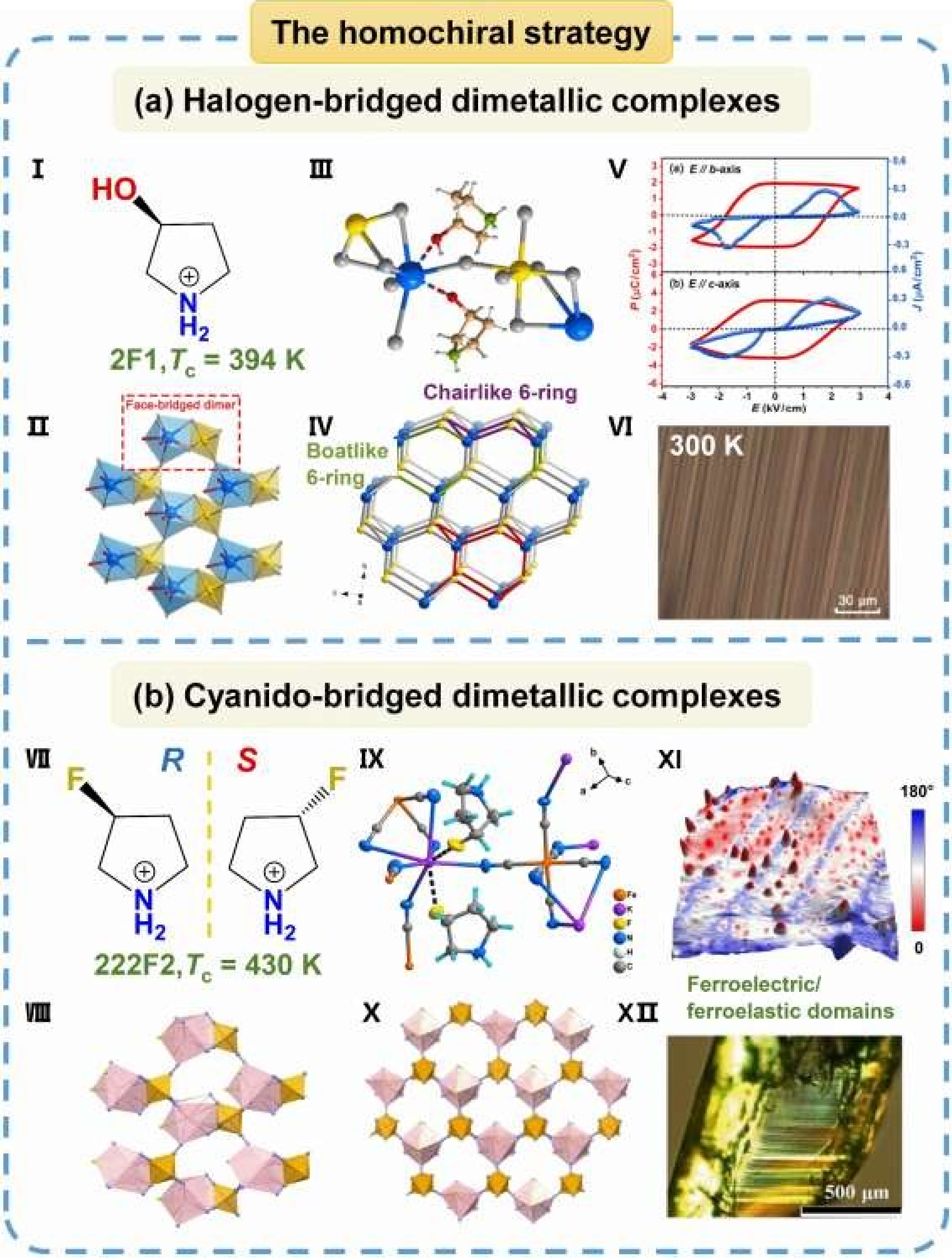

Fig.10 (a) The organic hybrid bimetal halide *R*-3HP with lonsdaleite topology: (I) The homochiral cation of (*R*)-3-hydroxypyrrolidinium. (II) Coordination polyhedral configuration of the inorganic framework viewed along the crystallographic bc-plane. (III) Its basic 3D cavity structure at 293 K. H atoms were omitted for clarity. (IV) Topological perspective view in which the straight lines and circles represent the Br ion ligands and Rb/Bi atoms, respectively. A basic unit of lonsdaleite topology was highlighted in red, and boat-like and chair-like six-rings in green and purple, respectively. (V) *P-E* hysteresis loop and J-E curve along *b*- and *c*-axis at room temperature. (VI) The ferroic domains at 300 K. (b) A pair of multiferroic chiral cyanido-bridged dimetallic complexes (*R*- and *S*-3-FPC): (VII) A pair of homochiral cation of (*R* and *S*)-3-fluoropyrrolidinium. (VIII) Coordination polyhedral configuration of the inorganic framework. (IX) Their basic 3D cavity structure. (X)

View Article Online
DOI: 10.1039/D5SC10231F

Topological perspective view. (XI) PFM phase superimposed on the 3D topographic image for *R*-3-FPC thin films measured at 298 K. (XII) Ferroelastic domain patterns at 393 K. Reproduced from ref. 61 and 62 with permission from American Chemical Society and Wiley, Copyright 2021 and 2022.

3.18 μC·cm^{-2} along the b- and c-axes, respectively. Its ferroelastic domain evolution with temperature and stress is visualized via PLM.Of note, (*R*-3HP)$_2$RbBiBr$_6$ displays fascinating CPL and semiconducting properties.

3D Cyanido-bridged dimetallic complexes

Cyanido-bridged dimetallic complexes are a common class of 3D non-perovskite structural compounds. Compared to the traditional 3D double perovskites (AB$_1^{\mathrm{I}}$B$_2^{\mathrm{III}}$X$_3$) with cage-like structures constructed from alternating corner-sharing [B$_1^{\mathrm{I}}$X$_6$] and [B$_2^{\mathrm{III}}$X$_6$] octahedrons, cyanido-bridged dimetallic complexes features the cyanide ions as a simple diatomic bridge ligand can link a variety of metal ions B^{x+} (such as Fe^{2+}, K^{+}, Co^{2+}, Na^{+}, Cr^{3+}) to assemble a periodic network with 3D hole structure. The significant advantage of this topology is its ability to accommodate larger organic cations, and the linear –B^{x+}–CN–B^{x+}–(– metal ion – cyanido – metal ion –) linkages provide highly structural flexibility. Therefore, in contrast to traditional perovskite analogues, where cation incorporation is strictly governed by the Goldschmidt tolerance factor and octahedral Jahn–Teller distortions are inherently limited, cyanido-bridged dimetallic complexes reveal highly tunable composition and structural diversity. Xiong group[62] reported the first pair of multiferroic chiral cyanido-bridged dimetallic complexes, [(*R*)- and (*S*)-3-fluoropyrrolidinium]$_2$[KFe(CN)$_6$] (*R*- and *S*-3-FPC) as shown in Fig.10b, where the chiral cations connect with K^{+} ions via the C-F…K interactions to form a unique 3D anion [KFe(CN)$_6$]$^{2+}$. Near 430 K, these materials undergo a reversible phase transition from the chiral-polar $P2_1$ to the chiral $C222_1$ space group, signifying a full ferroelectric and full ferroelastic transition (Aizu notation 222F2). The driving force of their phase transitions stems from the ordered-disordered transformation of R-3-fluoropyrrolidinium and S-3-fluoropyrrolidinium cations. Their inherent multiferroicity was rigorously established through PFM and PLM analyses. Particularly, *R*-3-FPC showcases outstanding ferroelectricity, with a saturated polarization reaching 9.4 μC·cm^{-2}. This research marks a crucial extension of multiferroic materials into the domain of chiral cyanido-bridged dimetallic systems.

5. Summary and outlook

Single-phase molecular multiferroics exhibit diverse applications due to the coupling between polarization and strain. For instance, in nonvolatile multistate memory, each storage unit can achieve multi-bit information by combining polarization orientation and strain states, enabling electric-write/mechanical-read or mechanical-write/electric-read modes, thereby significantly enhancing storage density; In high-precision actuators and brakes, the piezoelectric effect coupled with ferroelastic strain allows for electric-field-controlled precise displacement; In highly sensitive sensors, minute stress changes can be converted into easily detectable electrical signals; In shape-memory devices, regulating the stable state of ferroelastic domains via an electric field enables electrically controlled shape-memory functions, showing promise in fields such as micro-electromechanical systems (MEMS), robotics, and medical implants. How can such materials be efficiently designed and synthesized?

Based on the reported single-phase molecular multiferroic materials, a strategic approach focusing on composition and structure modulation is essential. For the organic components, molecules with low symmetry and high motional or rotational freedom are preferred. Chemical modifications of the organic components include halogen substitution, introduction of homochirality, incorporation of organo-functional groups, reduction of molecular rigidity, and alteration of molecular conformation. For the inorganic components, strategies including halogen substitution, metal-ion replacement, and doping with different elements to form solid solutions can be employed to modulate lattice distortion, electronic structure and phase transition behavior. These design principles collectively guide the synthesis of single-phase molecular multiferroics that meet the criteria for full ferroelectric and full ferroelastic coupling.

However, the development of this field still faces a series of challenges. First, single-phase molecular multiferroics that display strong polarization-strain coupling near room temperature remain scarce; most candidates operate at low temperatures or exhibit weak coupling. Second, the synthesis of molecular multiferroics still depends on trial-and-error approaches, falling far short of the function-by-design goal. There is an urgent need to establish an integrated database linking Aizu species, structures, and properties, and to combine first-principles calculations with machine-learning-driven high-throughput screening to discover superior candidates with high Curie temperatures and low coercive fields. Third, the theoretical foundation is incomplete. Extended theories capable of describing ferroelectric-ferroelastic and more complex order-parameter couplings (*e.g.*, ferrotoroidicity) are required, alongside the incorporation of non-Hermitian physics, topological phase transitions, and exploration of novel quantum-critical or nonequilibrium states. Moreover, precise dynamic control of coupled domains at the nanoscale remains technically limited; in-situ microscopy combined with phase-field simulations is needed to elucidate domain-wall dynamics and switching mechanisms. Finally, engineering-oriented research toward practical applications is crucial. Challenges in material fabrication, device processing, fatigue, and reliability must be overcome to translate laboratory breakthroughs into viable devices.

Looking forward, interdisciplinary collaboration and rational design are expected to enable the creation and deployment of high-performance single-phase molecular multiferroics, achieving breakthroughs in both material performance and application.

Author contributions

Meng-Meng Lun: Conceptualization, Investigation, Data curation, Visualization, Writing – original draft. Meng-Meng Sun: Investigation, Data curation, Writing – review & editing. Yong-Qiang Wang, Gao-Shang Gong, Mao-Cai Wei, Yu-Ling Su: Investigation, Writing – review & editing. Da-Wei Fu and Zun-Qi

Liu: Conceptualization, Supervision, Writing – review & editing, Funding acquisition. All authors approved the final version of the manuscript.

Conflicts of interest

There are no conflicts to declare.

Data availability

No primary research results, software, or code have been included, and no new data were generated or analysed as part of this review.

Acknowledgements

The authors gratefully acknowledge the support from the Key Research Project of Higher Education Institutions (26B140017) and Science and Technology Research Project (252102210203, 232102230121) of Henan Province. Natural Science Foundation of Henan Provincial (No. 262300422454).

References

1. H. Zheng and K. P. Loh, *Adv. Mater.*, 2024, **36**, e2308051.
2. Q. Pan, Z. X. Gu, R. J. Zhou, Z. J. Feng, Y. A. Xiong, T. T. Sha, Y. M. You and R. G. Xiong, *Chem. Soc. Rev.*, 2024, **53**, 5781-5861.
3. C. Y. Su, Y. F. Yao, Z. X. Zhang, Y. Wang, M. Chen, P. Z. Huang, Y. Zhang, W. C. Qiao and D. W. Fu, *Chem. Sci.*, 2022, **13**, 4794-4800.
4. D. W. Fu, H. L. Cai, Y. Liu, Q. Ye, W. Zhang, Y. Zhang, X. Y. Chen, G. Giovannetti, M. Capone, J. Li and R. G. Xiong, *Science*, 2013, **339**, 425-428.
5. Y.-Y. T. Heng-Yun Ye, Peng-Fei Li,, Wei-Qiang Liao, Ji-Xing Gao, Xiu-Ni Hua, Hu Cai, Ping-Ping Shi, Yu-Meng You and R.-G. Xiong, *Science*, 2018, **361**, 151–155.
6. W. Q. Liao, D. Zhao, Y. Y. Tang, Y. Zhang, P. F. Li, P. P. Shi, X. G. Chen, Y. M. You and R. G. Xiong, *Science*, 2019, **363**, 1206-1210.
7. Y. M. You, W. Q. Liao, D. Zhao, H. Y. Ye, Y. Zhang, Q. Zhou, X. Niu, J. Wang, P. F. Li, D. W. Fu, Z. Wang, S. Gao, K. Yang, J. M. Liu, J. Li, Y. Yan and R. G. Xiong, *Science*, 2017, **357**, 306-309.
8. H. Y. Zhang and R. G. Xiong, *Science*, 2023, **381**, 484-485.
9. P. Z. Huang, Z. Liu, L. K. Ye, H. F. Ni, J. Q. Luo, G. Teri, Q. Q. Jia, B. Zhuang, C. F. Wang, Z. X. Zhang, Y. Zhang and D. W. Fu, *Nat. Commun.*, 2025, **16**, 3071.
10. L. A. Gui, J. Chen, Y. F. Zhang, L. H. Li, J. R. Li, Z. B. Hu, S. Y. Zhang, J. Zhang, Z. Zhang, H. Y. Ye, Y. Peng, J. Ma and Y. Song, *Angew. Chem. Int. Ed.*, 2025, **64**, e202416380.
11. H. Zheng, A. Ghosh, M. J. Swamynadhan, Q. Zhang, W. P. D. Wong, Z. Wu, R. Zhang, J. Chen, F. Cimpoesu, S. Ghosh, B. J. Campbell, K. Wang, A. Stroppa, R. Mahendiran and K. P. Loh, *Nat. Commun.*, 2024, **15**, 5556.
12. Y. Liu, W. Guo, L. Hua, X. Zeng, T. Yang, Q. Fan, Y. Ma, C. Gao, Z. Sun and J. Luo, *J. Am. Chem. Soc.*, 2023, **145**, 16193-16199.
13. Q. Q. Jia, J. Q. Luo, Z. Y. Xue, J. S. Tang, W. Q. Qiu, C. F. Wang, Z. X. Zhang, H. F. Lu, Y. Zhang and D. W. Fu, *Chin. Chem. Lett.*, 2025, **36**,110471.
14. J. Valasek, *Phys. Rev.*, 1921, **17**, 475-481.
15. J. Valasek, *Phys. Rev.*, 1922, **20**, 639-664.
16. G. Busch and P. Scherrer, *Naturwissenschaften*, 1935, **23**, 737-737.
17. J. Jeong, H. S. Kim, G. Kwon, K. Jeong, H. Lee, J. H. Lee, M. Park, C. Lee, S. Yu, H. Kim, S. Im, K. Yoo, E. Lee and M. H. Cho, *Adv. Mater.*, 2022, **34**, e2108777.
18. M. M. Lun, J. Q. Luo, Z. X. Zhang, J. Li, L. Y. Xie, H. F. Lu, Y. Zhang and D. W. Fu, *Chem. Eng. J.*, 2023, **475**, 145969.
19. C. Shi, J. J. Ma, J. Y. Jiang, M. M. Hua, Q. Xu, H. Yu, Y. Zhang and H. Y. Ye, *J. Am. Chem. Soc*, 2020, **142**, 9634-9641.
20. Y. Z. Hu, L. You, B. Xu, T. Li, S. A. Morris, Y. X. Li, Y. H. Zhang, X. Wang, P. S. Lee, H. J. Fan and J. L. Wang, *Nat. Mater.*, 2021, **20**, 612-617.
21. G. Feng, Q. Zhu, X. Liu, L. Chen, X. Zhao, J. Liu, S. Xiong, K. Shan, Z. Yang, Q. Bao, F. Yue, H. Peng, R. Huang, X. Tang, J. Jiang, W. Tang, X. Guo, J. Wang, A. Jiang, B. Dkhil, B. Tian, J. Chu and C. Duan, *Nat. Commun.*, 2024, **15**, 513.
22. Z.-T. Xia, H.-P. Chen, J.-C. Qi, H. Peng, X. Shen, Y.-J. Bai, Z.-Y. Wang, T.-E. Yang and W.-Q. Liao, *Inorg. Chem. Front.*, 2025, **12**, 2825-2832.
23. T. Zhang, K. Xu, J. Li, L. He, D. W. Fu, Q. Ye and R. G. Xiong, *Natl. Sci. Rev.*, 2023, **10**, nwac240.
24. Y. F. Zhang, F. F. Di, P. F. Li and R. G. Xiong, *Chem. Eur. J*, 2022, **28**, e202102990.
25. L. Pan, H. F. Ni, P. Z. Huang, H. H. Li, M. J. Lin, G. Teri, J. Q. Luo, L. K. Ye, J. K. Xu, Q. Q. Jia, C. F. Wang, Z. Q. Liu, Z. X. Zhang, Y. Zhang and D. W. Fu, *Angew. Chem. Int. Ed.*, 2026, e5334832.
26. C. F. Wang, C. Shi, A. Zheng, Y. Wu, L. Ye, N. Wang, H. Y. Ye, M. G. Ju, P. Duan, J. Wang and Y. Zhang, *Mater. Horiz.*, 2022, **9**, 2450-2459.
27. H. F. Ni, L. Pan, C. H. Du, L. C. Xu, J. C. Lou, P. G. Liu, H. N. Wang, C. F. Wang, Z. X. Zhang, D. W. Fu and Y. Zhang, *Angew. Chem. Int. Ed.*, 2025, **64**, e202518937.
28. K. Aizu, *J. Phys. Soc. Jpn.*, 1970, **28**, 706-716.
29. J. Sapriel, *Phys. Rev. B*, 1975, **12**, 5128-5140.
30. K. Aizu, *J. Phys. Soc. Jpn.*, 1969, **27**, 387-396.
31. K. Aizu, *Phys. Rev. B*, 1970, **2**, 754-772.
32. H. Schmid, *J. Phys. Condens. Matter* , 2008, **20**, 434201.
33. R. E. Cohen, *Nature*, 1992, **358**, 136-138.
34. T. Y. Ju, C. C. Fan, B. D. Liang, C. D. Liu, M. L. Jin, C. Y. Chai and W. Zhang, *Adv. Funct. Mater.*, 2024, **34**.2316747.
35. I. B. Bersuker, *The Jahn-teller effect*, Cambridge Cambridge University Press, 2006.
36. J. Li, J.-F. Li, Q. Yu, Q. N. Chen and S. Xie, *J. Materiomics*, 2015, **1**, 3-21.
37. H. Y. Zhang, X. G. Chen, Y. Y. Tang, W. Q. Liao, F. F. Di, X. Mu, H. Peng and R. G. Xiong, *Chem. Soc. Rev.*, 2021, **50**, 8248-8278.
38. H. Y. Zhang, X. J. Song, X. G. Chen, Z. X. Zhang, Y. M. You, Y. Y. Tang and R. G. Xiong, *J. Am. Chem. Soc.*, 2020, **142**, 4925-4931.
39. K. Ding, H. Ye, C. Su, Y. A. Xiong, G. Du, Y. M. You, Z. X. Zhang, S. Dong, Y. Zhang and D. W. Fu, *Nat. Commun.*, 2023, **14**, 2863.
40. J. Y. Li, T. Zhang, M. M. Lun, Y. Zhang, L. Z. Chen and D. W. Fu, *Small*, 2023, **19**, e2301364.
41. Y. Ai, Z. B. Hu, Y. R. Weng, H. Peng, J. C. Qi, X. G. Chen, H. P. Lv, X. J. Song, H. Y. Ye, R. G. Xiong and W. Q. Liao, *Adv. Mater.*, 2024, **36**, e2407822.
42. H. P. Weber, B. C. Tofield and P. F. Liao, *Phys. Rev. B.*, 1975, **11**, 1152-1159.
43. M. M. Lun, C. Y. Su, J. Li, Q. Q. Jia, H. F. Lu, D. W. Fu, Y. Zhang and Z. X. Zhang, *Small*, 2023, **19**, e2303127.
44. Q. Q. Jia, G. Teri, Q. F. Zhou, J. Q. Luo, H. F. Ni, P. Z. Huang, P. G. Liu, L. Pan, C. F. Wang, Z. Liu, Z. X. Zhang, Y. Zhang and D. W. Fu, *Angew. Chem. Int. Ed.*, 2025, **64**, e202514669.
45. B. Zhuang, L. Pan, Z. L. Li, J. Y. Liu, Z. X. Zhang, K. Ding, Y. Zhang, Z. Q. Liu and D. W. Fu, *Acs Mater. Lett.*, 2025, **7**, 1540-1546.

View Article Online
DOI: 10.1039/D5SC10231F

46. J. Li, Y. Zhu, P. Z. Huang, D. W. Fu, Q. Q. Jia and H. F. Lu, *Chem. Eur. J.*, 2022, **28**, e202201005.
47. C. Y. Su, H. G. Yi, H. F. Ni, G. W. Du, S. Q. Xia, Z. Q. Liu, Z. X. Zhang and D. W. Fu, *Chem. Sci.*, 2025, **16**, 23385-23393.
48. Q. Q. Jia, G. Teri, J. Q. Luo, H. F. Ni, P. Z. Huang, M. M. Lun, Z. X. Zhang, Y. Zhang and D. W. Fu, *J. Am. Chem. Soc.*, 2024, **146**, 21120-21128.
49. Y. L. Zeng, Y. Ai, S. Y. Tang, X. J. Song, X. G. Chen, Y. Y. Tang, Z. X. Zhang, Y. M. You, R. G. Xiong and H. Y. Zhang, *J. Am. Chem. Soc.*, 2022, **144**, 19559-19566.
50. S. N. Li, R. J. Harrison, W. Li and M. A. Carpenter, *Chin. J. Chem.*, 2025, **43**, 3193-3198.
51. Y. Gao, M. Wu and P. Jena, *Nat. Commun.*, 2021, **12**, 1331.
52. X. J. Song, Y. Ai, X. G. Chen, Y. Qin, Y. Y. Tang, H. P. Lv, P. F. Li, H. Peng, Y. R. Weng, H. H. Chen, R. G. Xiong and W. Q. Liao, *J. Am. Chem. Soc.*, 2025, **147**, 16568-16577.
53. M. Ksiądzyna, A. Gągor, A. Piecha-Bisiorek, A. Ciżman, W. Medycki and R. Jakubas, *J. Mater. Chem. C*, 2019, **7**, 10360-10370.
54. L. Y. Zhan, Y. Zhou, N. Li, L. J. Zhang, X. J. Xi, Z. Q. Yao, J. P. Zhao and X. H. Bu, *J. Am. Chem. Soc.*, 2024, **146**, 5414-5422.
55. D. Fu, Z. Hou, Y. He, J.-C. Liu, H.-P. Lv and Y.-Y. Tang, *Chem. Mater.,* 2022, **34**, 3518-3524.
56. C. K. Yang, W. N. Chen, Y. T. Ding, J. Wang, Y. Rao, W. Q. Liao, Y. Y. Tang, P. F. Li, Z. X. Wang and R. G. Xiong, *Adv. Mater.*, 2019, **31**.
57. Y. L. Zeng, X. Q. Huang, C. R. Huang, H. Zhang, F. Wang and Z. X. Wang, *Angew. Chem. Int. Ed.*, 2021, **60**, 10730-10735.
58. N. Wang, Z. J. Xu, H. F. Ni, W. Luo, H. K. Li, M. L. Ren, C. Shi, H. Y. Ye, X. B. Fu, Y. Zhang and L. P. Miao, *Angew. Chem. Int. Ed.*, 2024, **63**, e202409796.
59. Q. Q. Jia, H. F. Lu, J. Q. Luo, Y. Y. Zhang, H. F. Ni, F. W. Zhang, J. Wang, D. W. Fu, C. F. Wang and Y. Zhang, *Small*, 2024, **20**, e2306989.
60. A. Sieradzki, M. Mączka, M. Simenas, J. K. Zaręba, A. Gągor, S. Balciunas, M. Kinka, A. Ciupa, M. Nyk, V. Samulionis, J. Banys, M. Paluch and S. Pawlus, *J. Mater. Chem. C*, 2018, **6**, 9420-9429.
61. L. He, P. P. Shi, L. Zhou, Z. B. Liu, W. Zhang and Q. Ye, *Chem. Mater.*, 2021, **33**, 6233-6239.
62. Y. Mao, X. G. Chen, Z. X. Gu, Z. X. Zhang, X. J. Song, N. Gu and R. G. Xiong, *Angew. Chem. Int. Ed.*, 2022, **61**, e202204135.
63. C. F. Wang, Y. Yang, Y. Hu, C. Ma, H. F. Ni, P. G. Liu, H. F. Lu, Z. X. Zhang, J. Wang, Y. Zhang, D. W. Fu, K. Zhao and Y. Zhang, *Angew. Chem. Int. Ed.*, 2024, **63**, e202413726.

View Article Online
DOI: 10.1039/D5SC10231F

Data availability

No primary research results, software or code have been included and no new data were generated or analysed as part of this review.